

Radio Spectral Index Variations and Physical Conditions in Kepler's Supernova Remnant

Tracey DeLaney, Barron Koralesky, and Lawrence Rudnick

*Department of Astronomy, University of Minnesota, 116 Church Street SE, Minneapolis,
MN 55455*

tdelaney@astro.umn.edu, barron@astro.umn.edu, larry@astro.umn.edu

John R. Dickel

Astronomy Department, University of Illinois at Urbana-Champaign, Urbana, IL 61801

johnd@astro.uiuc.edu

ABSTRACT

A new epoch of VLA measurements of Kepler's supernova remnant was obtained to make accurate measurements of the radio spectral index variations and polarization. We have compared these new radio images with $H\alpha$, infrared, and X-ray data to better understand the three dimensional structure and dynamics of Kepler, and to better understand the physical relationships between the various nonthermal and thermal plasmas. Spatial variations in the radio spectral index from -0.85 to -0.6 are observed between 6 cm and 20 cm. The mean spectral index is -0.71 . The mean percent polarization is 3.5% at 20 cm and 6% at 6 cm. There is a strong correspondence between the radial and azimuthal profiles of the radio, X-ray, $H\alpha$, and infrared emission in different locations around the remnant although there is no single, global pattern. Spectral tomography shows that the flat- and steep-spectrum radio emissions have distinct structures. The flat-spectrum radio emission is found either at a larger radius than or coincident with the steep-spectrum emission. We interpret these spectral components as tracing forward- and reverse-shocked material, respectively. The flat-spectrum radio emission can alternatively be interpreted as the bow-shocked material (reshocked by the forward shock) from the progenitor's motion through the interstellar medium. The $H\alpha$ and IR images are very similar. Their leading edges are coincident and are either in front of or coincident with the leading edges of the X-ray and radio emission. The X-ray emission matches the $H\alpha$ and IR emission in places, and in other places traces the steep-spectrum radio emission. In the north there is also an anticorrelation in the azimuthal profiles around the

remnant of the flat-spectrum radio emission and the thermal X-ray, $H\alpha$, and IR emissions. We suggest that this could be due to a relative weakening of the particle acceleration at the forward shock due to Alfvén wave damping in regions of high density.

Subject headings: supernova remnants — ISM: individual (Kepler’s SNR) — radio continuum: ISM

1. Introduction

Kepler’s supernova remnant (SNR; G4.5+6.8, SN 1604) is the second youngest SNR known in the Galaxy. Recent distance estimates (Reynoso & Goss 1999) place the remnant between 4.8 and 6.4 kpc (we adopt 5 kpc for our calculations) and it is about $200''$ (≈ 4.8 pc) in diameter. As a young, bright SNR, it has been studied at many wavelengths. The most recent study comparing the radio, X-ray, optical, and infrared (IR) emission was conducted by Braun (1987) at a resolution of $2'$. It is time to revisit this analysis using the most recent observations and at a higher resolution.

The radio emission has a shell-like morphology and is brighter in the north than in the south. The radio emission results from synchrotron radiation which probes the interaction between relativistic particles and the magnetic fields. Shocks and eddy motions at Rayleigh-Taylor instabilities are thought to provide the necessary acceleration mechanism and magnetic field enhancement to produce the synchrotron emission (Gull 1973).

SNRs are thought to be the primary acceleration sites for Galactic cosmic rays below $\approx 10^{14}$ eV. The acceleration process is probably first- or second-order Fermi acceleration in the shocks and/or turbulence from the supersonic expansion of the supernova ejecta (Jones *et al.* 1998). Many details of the acceleration process are not well established observationally. For instance, we do not know what constitutes the seed population of particles for the acceleration mechanism nor how these particles are injected into the cycle. By observing the radio spectral index, α ($S_\nu \propto \nu^\alpha$), of the synchrotron radiation from the relativistic electrons, we can determine local shock and dynamical characteristics (Anderson *et al.* 1991; Anderson & Rudnick 1993, 1996; Katz-Stone *et al.* 2000).

The X-ray emission has the same shell-like morphology and is qualitatively similar to the radio emission with the same north-south brightness asymmetry (Matsui *et al.* 1984). The X-ray emission results from two processes. The first is line emission from heavy elements and the second is bremsstrahlung emission from a hot thermal plasma. At the energies covered by the ROSAT HRI ($\lesssim 2$ keV), ASCA observations indicate that Kepler’s spectrum includes

the Fe L line complex and the lines of Mg XI $K\alpha$ and Si XIII $K\alpha$ (Kinugasa & Tsunemi 1999). At energies $\lesssim 1.4$ keV, there is also confusion between the unresolved Fe L line complex and the thermal continuum.

Using EINSTEIN and ROSAT HRI images, Hughes (1999) measured the X-ray expansion parameter m (defined as $R \propto t^m$) to be 0.93 which indicates that the remnant is nearly in free expansion. The radio expansion parameter is ≈ 0.5 (Dickel *et al.* 1988) which is only about half that of the X-ray. The disparity between radio and X-ray expansion appears to be a common theme in young SNRs as the same behavior has been found in Cassiopeia A (Koralesky *et al.* 1998) and Tycho’s SNR (Hughes 2000).

The most recent optical images are over ten years old (Blair *et al.* 1991; Bandiera & van den Bergh 1991); however, the slow expansion of the optical remnant, ≈ 200 km s $^{-1}$ (Bandiera & van den Bergh 1991), allows comparison to newer images at radio, X-ray and IR wavelengths. The optical remnant consists of diffuse filaments and bright knots. The emission is concentrated to the north and northwest with some structures near the center of the remnant. Observations indicate both radiative and nonradiative (Balmer-dominated) emission (Fesen *et al.* 1989; Blair *et al.* 1991). The radiative emission is mostly concentrated in the knotty structures in the northwest, where the brightness in all emission lines is strongest, while the Balmer-dominated emission is associated with filamentary structures and a few knots. The Balmer-dominated spectrum consists of both broad and narrow components. This type of spectrum results from a high velocity shock passing through a low density, partially neutral medium. The broad component specifically results from a charge exchange reaction between slow neutral atoms and fast protons *behind* the shock (Chevalier *et al.* 1980). Balmer-dominated emission is referred to as nonradiative because the radiative timescale behind the shock is long in comparison with the dynamical time scale. The inferred shock velocity is ≈ 1800 km s $^{-1}$. The observed [S II] line ratios indicate that the optical filaments have very high densities ($n_e \geq 1000$ cm $^{-3}$) compared with other galactic SNRs (Dennefeld 1982).

Observations in the IR are important because this emission is thought to be the dominant cooling mechanism in SNRs (Draine 1981). The most recent IR study has been conducted with ISO (Douvion *et al.* 1999, 2001). The IR continuum emission is consistent with a 120 K blackbody. There are also some weak [Ne II] or [Ar II] ionic lines in the brightest regions of the remnant. Spatially, the IR emission is strongly correlated with the H α emission and is thought to be thermal emission from shock heated dust in the circumstellar region.

Kepler’s progenitor is somewhat of an enigma. Baade (1943) identified the remnant as the remains of a type I supernova and its distance above the Galactic plane (≈ 600 pc) is consistent with a population II progenitor, suggesting a type Ia event. Also, recent ASCA

observations (Kinugasa & Tsunemi 1999) indicate a relative overabundance of iron that agrees with type Ia supernova nucleosynthesis models. However, the nitrogen overabundance in the optical knots (Dennefeld 1982), the slow expansion velocities of these knots, and the enhanced density in the region suggest that they are circumstellar material ejected by the stellar wind from a massive star. Bandiera (1987) proposed a model suggesting that the progenitor was a massive runaway star. This model also explains the observed north-south brightness asymmetry as a blast wave presently moving through the bow shock (the brighter northern rim) in the direction of the progenitor’s motion. Borkowski *et al.* (1992) performed numerical simulations which showed that the model recovered the observed morphology of Kepler’s SNR.

In this paper we wish to provide an improved look at the radio structure, spectral variations and polarization properties, as addressed earlier by Dickel *et al.* (1988) and Matsui *et al.* (1984). We also look in more detail at the relationship between the radio emission and those at optical, IR, and X-ray wavelengths. In §2 of the paper we describe the radio observations and data reduction. In §3 we present the various images made from the radio data, discuss how they were made, present some statistics, and describe features on these images. The optical, IR, and X-ray images are presented in §4 along with descriptions of features on these images. Comparisons between the various radio images and the optical, IR, and X-ray images are presented in §5 with discussion in §6 and concluding remarks in §7.

2. Radio Observations and Data Reduction

Observations were made with the VLA¹ using all four configurations from the most extended A-configuration with a maximum antenna separation of 36.4 km to the most compact D-configuration with a shortest separation of 35 m. These are summarized in Table 1. Data were taken at 4835.1 and 4885.1 MHz (hereafter called 6 cm) and at 1285.0, 1365.1, 1402.5, and 1464.9 MHz (hereafter called 20 cm).

Standard calibration procedures were used for the 6 cm data and most of the 20 cm data as described in the AIPS Cookbook². There were two exceptions to this at 20 cm. First, at A configuration, no flux density and polarization data for the primary calibrator were available with the same observational parameters as the source. We therefore set the

¹The VLA is operated by the National Radio Astronomy Observatory, which is a facility of the National Science Foundation, operated under cooperative agreement by Associated Universities, Inc.

²<http://www.cv.nrao.edu/aips/cook.html>

flux density scale using a value of 1.3 Jy for the phase calibrator, J1751-2524 (VLA online calibrator manual³). The flux density of J1751-2524 at B and C configuration, determined by comparison with the primary flux density calibrator, varies from 1.3 Jy by as much as 0.05 Jy depending on the frequency. Therefore, a possible calibration error of up to 4% was introduced into the 20 cm A-configuration data.

To determine the absolute polarization position angle, a comparison was made between polarization images made separately for A- and B-configuration data, tapered to the same resolution. Forcing the angles to be the same in the high signal-to-noise regions resulted in a possible position angle error of up to 3° for the 20 cm, A-configuration data.

The second problem was at D configuration where there was insufficient parallactic angle coverage to solve for the instrumental and source polarization terms for the phase calibrator. In this case, the instrumental polarization solutions were obtained by assuming that the flux density and phase calibrators had the same polarization as when they were observed in B and C configuration. The rms phase errors for the polarization calibrator were less than 5° after this correction.

After initial calibration, multiple passes of self-calibration were performed to improve the antenna phase solutions. For the 6 cm data, the first few passes of self calibration at B configuration (the largest configuration size at this frequency) were done using a shorter spatial frequency range. The final pass of self-calibration used the entire spatial frequency range and included an amplitude calibration. In order to facilitate comparison between 6 cm and 20 cm, the final 6 cm images were made with a similar beam shape and size as that at 20 cm and the maximum spatial frequency range was set to that at 20 cm. The AIPS maximum-entropy deconvolution routine VTESS, which maximizes smoothness in an image within the confines of the data, was used to restore the total intensity images using a zero-spacing flux density estimate of 6.3 Jy which was the total flux density reported by Dickel *et al.* (1988) for their 6 cm image. The default image for VTESS was a 6 cm image convolved to C-configuration resolution. The standard correction for primary beam attenuation was applied to the final 6 cm images. This correction raised the flux density at the outermost edge of the remnant by 6%.

For the four frequencies at 20 cm, a shorter spatial frequency range was again used to self calibrate the A-configuration data before doing a pass using the entire spatial frequency range. A final calibration was done in phase only using a flux-density-scaled 6 cm image. Although self-calibration improves antenna phase, absolute position information is degraded. Using the 6 cm image to calibrate in phase effectively registers one image to the other. To

³<http://www.aoc.nrao.edu/~gtaylor/calib.html>

solve the problem of an extended plateau in the beam pattern at low levels (Matsui *et al.* 1984), the spatial frequency coverage weighting parameters in IMAGR were adjusted to provide a clean Gaussian beam. The minimum spatial frequency range was also set to that at 6 cm. The final 20 cm images were deconvolved using VTESS with the same default as that used at 6 cm but with the flux density scaled to 20 cm. This essentially requires VTESS to make the 20 cm image look as much like the 6 cm image as possible with any resulting differences being due to the requirements of the data. Variations in spectral index then result from significant differences in the data between 6 cm and 20 cm instead of the reconstruction algorithm. A zero-spacing flux density estimate of 17 Jy was used for image reconstruction in VTESS. This value was also chosen to match that used by Dickel *et al.* (1988) who added the 17 Jy to their data before image construction. The final images at 20 cm were corrected for primary beam attenuation which raised the flux density at the outer edge of the remnant by 0.5%.

The AIPS routine UTESS, which maximizes emptiness in an image within the confines of the data, was used to restore Stokes Q and U images at 6 cm and 20 cm. The input images were made using IMAGR with the same spatial frequency coverage and weighting as used for the total intensity images. No default images or zero-spacing flux density estimates were used for reconstruction. The final images were corrected for primary beam attenuation.

The images have been convolved to a $7''.2$ round beam for several reasons. First, Kepler’s SNR is very far south for the VLA ($\delta_{2000} \approx -21^\circ.5$) so the north-south antenna spacings are foreshortened to produce a very elliptical beam. Second, in trying to make the 20 cm beam Gaussian, the beam size had to be increased resulting in a major axis of nearly $3''.6$. Third, even with a $3''.6$ round beam, the 20 cm images had a rippling feature similar to sidelobe emission from a distant bright source which could not be eliminated. Finally, using a larger beam increased the signal-to-noise ratio. The higher resolution images were used in our proper motion study (B. Koralesky, L. Rudnick, & T. DeLaney, in preparation).

3. Radio Images

3.1. Total Intensity

Representative 20 cm (1285 and 1365.1 MHz combined as described in §3.2.1) and 6 cm (4835.1 MHz) total intensity images are shown in Figures 1 and 2, respectively. Table 2 summarizes the integrated flux densities and rms noises of the final total intensity images. The flux densities agree to within 5% of flux densities interpolated from the data compiled by Reynolds & Ellison (1992).

The total intensity images at 6 cm and 20 cm show the same features described by Matsui *et al.* (1984) and Dickel *et al.* (1988). Kepler’s SNR is a shell type with the northern portion of the ring about 3 times brighter than the southern portion of the ring. The thickness of the northern portion of the ring is $\approx 25''$ and the radius of curvature of this bright ring deviates from circular symmetry in the northwest. For reference, the Galactic plane is 6.8° southeast of the remnant running from approximately northeast to southwest.

We now define nomenclature that will be used elsewhere in this paper to refer to spatial regions in Kepler’s SNR. These regions are shown schematically on Figure 2. The “northern ring” and “southern ring” refer to the limb-brightened shell. The protrusion separating the northern ring from the southern ring in the east is called the “eastern ear” and the similar protrusion in the west is called the “western ear.” The “central band” is the emission ridge extending from the southeast to the central part of the remnant and “steep arc” refers to the ridge of emission crossing from east to west in the northern half of the remnant. The small protrusion at -25° is called the “bump” and the interior feature located just north of the southern ring at -115° is called the “western stub.”

3.2. Spectral Index

3.2.1. Variations Across the Remnant

For the spectral index measurements, two independent maps were made at each of the 20 cm and 6 cm bands. The first spectral index map (pair 1) consisted of data from 1285 and 1365.1 MHz (20 cm), and 4835.1 MHz (6cm). The second spectral index map (pair 2) consisted of data from 1402.5 and 1464.9 MHz (20 cm), and 4885.1 MHz (6cm). The differences in spectral index between the two independent images were small, except at low signal-to-noise. These images were therefore blanked when the 20 cm flux density was less than $5 \text{ mJy } \text{bm}^{-1}$. Figure 3 shows the consistency between the two spectral index measurements. To eliminate oversampling, only values of pixels that are separated by one full beamwidth are displayed. After blanking, the rms difference between the two independent spectral index images is ± 0.019 . The two spectral index images were then averaged together to make the final spectral index image which is shown in Figure 4. The color is determined by the spectral index and the intensity is set by the 6 cm (4835.1 MHz) continuum radio image.

For the first time reliable spectral index variations have been measured in the remnant between 6 cm and 20 cm. The spectral index ranges from -0.85 to -0.6 . However, the spectral index in Figure 4 ranges from -0.85 to -0.65 to better enhance the details. To

assess the reliability of the variations in the final spectral index image, a continuous flat spectral region in the northern ring and a continuous steep spectral region in the western ear and western stub were chosen from the total intensity images (pair 1). The regions chosen are about 2700 arcsec^2 in area representing about 50 independent beams each. Figure 5 is the plot of $\log(I_6/I_{20})$ vs. $\log(I_{20})$ where I_x is the intensity in band x for each region. There is a distinct separation between the flat and steep components, much greater than the scatter and showing no significant biases as a function of intensity.

As a test to determine if the measured spectral index variations could reproduce the observed small curvature in the integrated spectrum (Reynolds & Ellison 1992), the total 20 cm (using pair 1) flux density at each spectral index was measured and binned, as shown in Figure 6a. These binned data were then used to predict the integrated flux densities at other frequencies by summing the flux density contributions determined for each spectral index box assuming each spectral index bin represented a different power law fixed to its observed flux density at 20 cm. The predicted spectrum is shown as the solid line in Figure 6b. The data points and error bars in Figure 6b were taken from Reynolds & Ellison (1992) and trace out the observed integrated spectrum. Although the spectrum predicted from our superposed power laws model shows small positive curvature, it is insufficient to describe the current data between 10 MHz and 10 GHz. Thus there must be some mechanism, such as the cosmic ray modification of shocks proposed by Reynolds & Ellison (1992), that produces the positive curvature in the spectrum.

3.2.2. Mean Spectral Index

Although we are primarily interested in spectral index variations, for completeness we have also determined the mean spectral index. We use two methods. The first is to determine the mean value in the spectral index image which yields a value of -0.71 with a formal error in the mean of 0.001 . The second method uses the integrated flux densities at 6 cm and 20 cm (using the mean spectral index value from pair 1 and pair 2) and yields the same value. The actual errors in the mean spectral index are dominated by calibration errors, yielding an estimated uncertainty of $\approx 2\%$ and by the missing flux density from the interferometer's lack of sensitivity to the largest scale emission. Since the spatial frequency sampling of the 6 cm and 20 cm images were matched for our spectral index analysis, we expect the same degree of missing flux density at each waveband. We cannot assign an error to the missing flux density because modern single dish flux density measurements are not available. Our results differ from the mean spectral index of -0.65 reported in Dickel *et al.* (1988). We believe the earlier results are less reliable because of their poorer available interferometer

sampling, and the use of data from only the bright northern ring, which we found to be flatter than average.

3.2.3. Spectral Tomography

Because the radio emission is optically thin, it is possible that some of the measured spectral variations can be confused by overlapping structures. Spectral tomography is a technique designed to separate such structures. This technique has been applied to analyze the spectra of radio galaxies (Katz-Stone & Rudnick 1997) and, recently, to Tycho’s SNR (Katz-Stone *et al.* 2000). Because the spectral index of the overlapping components is not known, a gallery of images is made each with a specific spectral component subtracted out. Mathematically, a set of images $M_t(\alpha_t)$ is constructed where,

$$M_t(\alpha_t) \equiv M_{20} - M_6 \left(\frac{\nu_{20}}{\nu_6} \right)^{\alpha_t},$$

where $M_{6,20}$ are the images at 6 cm (4835.1 MHz) and 20 cm (using pair 1). If a component has spectral index α_t , it will disappear with respect to its surroundings in image M_t . If a component has spectral index $> \alpha_t$, it will be oversubtracted and have negative brightness. If a component has spectral index $< \alpha_t$, it will be undersubtracted and have positive brightness. Note that the tomography images are intensity weighted as well as showing spectral index changes.

Figure 7 consists of two images from the tomography gallery. The image on the left (hereafter called flat) is the result of setting $\alpha_t = -0.75$ and represents a flat component of emission. For display purposes, this image has been reversed so that what is actually shown is $-M_{-0.75}$; therefore bright spatial components are flatter in spectral index than this value. Essentially all of the steep emission has been subtracted out to give zero or negative brightness values at the locations of those features, with the steepest features in the west substantially oversubtracted. What shows up as positive brightness results from emission flatter than $\alpha_t = -0.75$. The image on the right (hereafter called steep), for $\alpha_t = -0.65$, has the flatter component subtracted out so that positive brightness represents emission steeper than $\alpha_t = -0.65$ and negative brightness represents flatter emission.

Prominent features on the flat-spectrum radio image include the northern ring and a thin southern ring. Many of the interior features have disappeared and the eastern ear is very faint. The western side of the remnant (western ear and western stub), the bump, and parts of the central band have been oversubtracted in the flat image but are prominent in the steep-spectrum radio image. The eastern ear is relatively more defined in the steep

image than in the flat image. Parts of the northern and southern ring are also steep and the steep arc is clearly defined in the steep-spectrum radio image. When we refer to structures as flat, they appear prominently in the flat image and they are predominantly green or blue in Figure 4. Similarly, when we refer to structures as steep, they appear prominently in the steep image and they are predominantly yellow, orange, or red in Figure 4. It would be an oversimplification to state that the remnant consists of exactly two overlapping spectral components. Many areas of the remnant show a spectral index gradient indicating that the remnant is likely composed of multiple overlapping spectral index structures rather than just two structures.

3.3. Polarization Results

3.3.1. Polarized Intensity

Noise corrected linearly polarized intensity (POLI) images for one frequency at 6 cm (4835.1 MHz) and one frequency at 20 cm (1365.1 MHz) were made from the Stokes Q and U images using the AIPS routine COMB. These images, and the fractional polarization (FPOL) images are shown in Figure 8. The fractional polarization image at 6 cm was blanked based on intensity values below $0.5 \text{ mJy } \text{bm}^{-1}$ on the 6 cm total intensity image while the 20 cm fractional polarization image was blanked below $2 \text{ mJy } \text{bm}^{-1}$ on the 20 cm total intensity image. The northern and southern rings and ears are clearly identified in the polarization intensity images although the north-south brightness asymmetry is not as pronounced as it is in the total intensity images. The interior structures, excepting the central band, are not at all defined and the bump is also difficult to discern in the polarized intensity images.

In order to determine the mean percent polarization in the remnant, two definitions will be used because they weight the polarized emission differently. The first is $\langle P_x \rangle$ where the P_x are the pixel values from the fractional polarization images for band x in Figure 8. Using this definition, $\langle P_6 \rangle = 6.1 \pm 0.1\%$ while $\langle P_{20} \rangle = 3.8 \pm 0.1\%$. The second method for determining the “mean” percent polarization is to calculate $\Sigma \text{POLI}_x / \Sigma I_x$ where POLI is polarized intensity, the x ’s are defined as before, and the sums refer to integrated intensities on unblanked images. Based on this definition, $\Sigma \text{POLI}_6 / \Sigma I_6 = 6\%$ and $\Sigma \text{POLI}_{20} / \Sigma I_{20} = 3.5\%$ which are close to the values measured by $\langle P_6 \rangle$ and $\langle P_{20} \rangle$. In comparison, Matsui *et al.* (1984) report $\Sigma \text{POLI}_x / \Sigma I_x = 4.4\%$ and 2.2% for 6 cm and 20 cm, respectively. We have examined a number of possibilities for why our values differ from those of Matsui *et al.* (1984) but we cannot identify the cause of the discrepancy without reevaluating the 1984 data.

The degree of polarization is an important measure in SNRs because it is an indicator

of the magnetic field ordering and the ratio of fractional polarizations at different bands is a measure of the mixing of synchrotron and thermal plasmas. For a uniform magnetic field, the degree of polarization of a synchrotron source is independent of frequency and is directly related to the spectral index by $P = (3 - 3\alpha)/(5 - 3\alpha)$. For Kepler’s mean spectral index of -0.71 , the mean percent polarization should be about 72%. In order to account for the low percent polarization in Kepler’s SNR, as well as other young SNRs (Milne 1987), the magnetic field must have a high degree of disorder on subarcsecond scales.

3.3.2. Depolarization

Another effect that further depolarizes SNRs at longer wavelengths is differential Faraday rotation of emission from regions at different depths in the SNR. Figure 9 is a depolarization (P_{20}/P_6) image showing variations over the full range of 0 (complete depolarization) to 1 (no depolarization). The image has been blanked based on the 6 cm polarized intensity of 0.3 mJy bm^{-1} below which noise becomes important. A north-south asymmetry is apparent here as portions of the bright northern ring are strongly depolarized while the southern ring shows little depolarization.

3.3.3. Faraday Rotation and Magnetic Field

Because the Faraday rotation is dependent on λ^2 , we can determine it by combining the position angles of the polarization vectors at multiple wavelengths. To do this, average Stokes Q and U images were calculated at 20 cm (using the 1365.1, 1402.5, and 1464.9 MHz images) and at 6 cm (using both frequency images), and then used to construct 20 cm and 6 cm polarization angle images. An angle difference image was constructed between 20 cm and 6 cm. The angle difference image was blanked based on the 20 cm polarized intensity of 0.4 mJy bm^{-1} below which noise becomes important and was then used to calculate the rotation measure image. The angle difference image had to be corrected for 180° ambiguities. To do this, a critical assumption was made that there should be no abrupt, large angle difference jumps from one pixel to the next in the image. Therefore, small scale “jump” regions were shifted 180° to conform to the larger surrounding regions. By constraining the image to have smooth transitions between regions, the total range of angle differences is found to be larger than 180° . The procedure of assuming no sudden jumps of 180° appears to produce a unique result, except for an overall 180° ambiguity for the entire image. This ambiguity is removed by looking at the angle difference between two 20 cm (1365.1 and 1464.9 MHz) polarization angle images. A rotation measure image was also made using the AIPS routine RM, which

does not involve application of the no-jump criterion. The resulting image had only a few minor differences from the manually constructed rotation measure image after appropriate blanking for noise.

The final rotation measure image is shown in Figure 10 and reveals the same north-south asymmetry seen elsewhere. The western ear has more positive rotation measures than the rest of the remnant while the southern ring has the most negative rotation measures in the remnant. There is also a steep gradient in rotation measure across the bump. These results correspond well with those presented in Matsui *et al.* (1984), although they do not allow variations larger than 180° across their image. Since we do not expect the external Faraday screen to vary substantially over the angular size of Kepler’s SNR ($\approx 200''$) (Simard-Normandin & Kronberg 1980), the range of rotation measure from -67.7 rad m^{-2} to 27.7 rad m^{-2} is probably the result of variations in plasma density and thickness and magnetic field strength and orientation within the remnant as pointed out by Matsui *et al.* (1984).

Figure 11 shows the magnetic field structure in the remnant, after correction for the derived rotation measure. All vectors have been set to the same length. The contours are 6 cm radio continuum. The magnetic field is radial for the most part, as seen in other young SNRs (Milne 1987), but there are significant deviations from radial on scale sizes of $\approx 20''$. In general, there is more disorder in the south than the north as noted by Matsui *et al.* (1984) for their polarization angle images. Recent proper motion measurements show many of the same patterns as the magnetic field structure (B. Koralesky, L. Rudnick, & T. DeLaney, in preparation).

4. Optical, Infrared, and X-ray Images

An $\text{H}\alpha + [\text{N II}]$ (hereafter just $\text{H}\alpha$) image was obtained by Blair *et al.* (1991) and kindly provided to us by W. Blair. This image was taken in 1987 with the 2.5 m DuPont telescope at Las Campanas. The stars on this image were already removed to first order by subtracting a continuum image. There were enough intact stellar remnants, though, to register the $\text{H}\alpha$ image to the stars on a DSS image to an accuracy of better than $1''.5$.

In order to compare the distribution of $\text{H}\alpha$ to our radio images at a resolution of $7''.2$, we had to take an extra step to further remove significant contributions from stars. The stars embedded in the $\text{H}\alpha$ emitting regions were identified by detailed comparisons with images by D’Odorico *et al.* (1986) and Bandiera & van den Bergh (1991) and “removed” by replacing the pixel intensities with that of nearby, diffuse $\text{H}\alpha$ emission in the same regions. To remove stars that were not embedded in emission, the local mean was determined for

a region immediately adjacent to each star. These stars were then “removed” by replacing their pixel intensities with the local mean. Our final convolved $H\alpha$ image is shown in Figure 12 with a square root transfer function to enhance the faint emission.

Although the $H\alpha$ image is ten years older than those at the other wavelengths, this is not a problem because of the small proper motions of $H\alpha$ features. The fastest moving knot in right ascension would have moved $0''.384$ and the fastest moving knot in declination would have moved $0''.367$ in ten years (Bandiera & van den Bergh 1991). These are well within the registration errors.

An IR image was obtained by Douvion *et al.* (1999, 2001) and kindly provided to us by P.-O. Lagage and T. Douvion. This image represents data taken in 1996 with the LW8 filter (10.7-12 μm) aboard ISO. The IR image was registered in the same manner as the $H\alpha$ but using a 2MASS image as the template and yielding, again, a positional uncertainty of $1''.5$. Due to the resolution of ISO ($6''$), individual stars in the emitting regions could not be isolated and removed. The final image is shown in Figure 12 and was convolved to $7''.2$ for comparison to the other wavelength images.

To make the X-ray image shown in Figure 12, the ROSAT high resolution imager data taken in 1997 and used by Hughes (1999) were obtained from the ROSAT public archive. An image was made at $1'' \text{ pixel}^{-1}$ using the program FTOOLS and then convolved with a $7''.2$ beam. The registration of the X-ray image is not a straightforward process. Unlike the IR, there are no groundbased observations at X-ray energies to establish an absolute coordinate system. It is also unclear exactly what the spatial relationship is between the X-rays and emission at other wavelengths. Typically, X-ray images have been registered to radio images because of the similar distribution of the diffuse emission and the general similarity of the locations of large-scale bright regions. A comparison of the X-ray and $H\alpha$ images, though, clearly shows several features common to both such as the emission at the center, in the northwest, and the northeast (outlined in red on Figure 12). Given these specific regions of similarity, the X-ray image was registered by maximizing the correlation of emission with the $H\alpha$ image. This was done by spatially shifting one image with respect to the other and assuming that there were no rotation or scaling differences between the two images. A difference image was constructed for each position shift. The final shift position was set when the residuals for each of the “similar” regions were minimized. The positional uncertainty between the two images is $1''.5$. To determine how different the position of the X-ray image could have been if we had registered to a radio image instead, angle averaged radial brightness profiles for the radio total intensity and X-ray images were created using the same parameters as the comparison by Matsui *et al.* (1984) who registered their Einstein HRI image to their radio total intensity image. The relative positions of our X-ray and radio

total intensity images agree to within $2''$ with the Einstein HRI and radio registration of Matsui *et al.* (1984).

The X-ray and $H\alpha$ images show a general north-south brightness asymmetry. Although the IR image has no data in the south, IRAS observations (Braun 1987) indicate the same north-south brightness asymmetry as seen in the other wavebands. The $H\alpha$ and IR images are remarkably similar. Both images are brightest in the northwest, have a “gap” in the north corresponding to reduced surface brightness, have emission corresponding to the central band, have a clearly defined bump, and have emission slightly west of center. The reader is reminded that the $H\alpha$ image includes [N II] emission and, in fact, spectra taken by Blair *et al.* (1991) indicate that the bright northwest region is probably dominated by [N II] emission. The X-ray image has emission which corresponds to the emission on the $H\alpha$ and IR images. However, there are regions of dissimilarity as well. Unlike the $H\alpha$ and IR, the X-ray emission has a much less pronounced gap in the north and the ears and southern ring are clearly defined (with the caveat that there are no data in the south for the IR image). The reader is also reminded that the comparison here involves X-rays at energies $\lesssim 2$ keV. No statement is implied about the distribution of X-ray emission at higher energies.

5. Comparisons

The most striking aspect of all of the images presented in this paper is the north-south asymmetry. This is seen in brightness (Figure 12), spectral index (Figure 4), polarization (Figure 8), depolarization (Figure 9), and rotation measure (Figure 10). Other interesting features include the bump which is distinctly visible in the brightness images in all wavebands, has a steep radio spectrum, and has a rotation measure gradient. The very steep western ear is not prominent in either the $H\alpha$ or IR images, is not depolarized, but has the most positive rotation measures. In contrast, the somewhat steep eastern ear has negative rotation measures but shares all the other properties of the western ear.

The correlation between thermal emission and both depolarization and rotation measure is expected since Faraday rotation is proportional to the integral of thermal electron density times magnetic field along the line of sight and both bremsstrahlung and line emission are proportional to the square of the electron density. The relation between depolarization and X-ray emission can be seen in Figure 13. The data were binned by their depolarization with 45 independent beams per bin. The \times 's and the error bars show the mean and error in the mean of the X-ray brightness in each depolarization bin. Figure 14 is a similar plot for rotation measure and X-ray emission with the data binned by rotation measure into 50 independent beams per bin. Data from the western ear dominates the region with rotation

measures greater than 0 rad m^{-2} while data from the southern ring dominates the region with rotation measures less than -20 rad m^{-2} . The region between -20 and 0 rad m^{-2} contains data primarily from the bright northern ring and the less bright interior of the remnant. If the western ear and the interior of the remnant are excluded, then there is a clear correlation between rotation measure and X-ray brightness as reported by Matsui *et al.* (1984). To determine where zero rotation actually lies, so that it can be determined if more rotation corresponds to brighter X-ray regions, the galactic contribution to the rotation measure must be removed. Because Kepler’s SNR is about 600 pc above the galactic plane, we assume that all of the galactic Faraday screen in that section of the sky lies between us and Kepler. Using the catalog of Broten *et al.* (1988), the median rotation measure of all extragalactic sources within 20° of Kepler’s SNR (21 sources) is 5 rad m^{-2} excluding two sources with rotation measure beyond 2σ . However, the rms of the remaining 19 sources is 77 rad m^{-2} which is too large to allow a reliable determination of the galactic contribution to the rotation measures in Kepler’s SNR. There is thus no way to test whether X-ray brightness is related to more or less rotation.

In Figure 15 we plot angle-averaged radial profiles for the $\text{H}\alpha$, IR, X-ray, and 6 cm (4835.1 MHz) radio total intensity emission in three sectors of the remnant. In Figure 16, angle-averaged radial profile plots of the X-ray and steep- and flat-spectrum radio emission are shown for the same sectors. There is a strong correspondence between these different emission components, but it varies from sector to sector. Some of the key patterns are as follows: 1. The $\text{H}\alpha$ and IR have the same distribution (NNE, NW). 2. The $\text{H}\alpha$ and IR are either in front of the X-ray and radio emission (NNE) or at the same leading edge (NW). Note that the leading plateau of radio emission comes from parts of the western ear, not the bright shell. 3. The X-ray emission corresponds in size, shape, and position to either one of the radio components (flat, NW; steep, S) or both (NNE). 4. The flat-spectrum radio emission is either in front of (NW, S) or coincident with (NNE) the steep-spectrum radio emission. For reference, circles $100''$ in radius and centered at $\alpha_{2000} = 17^{\text{h}}30^{\text{m}}41^{\text{s}}.25$ and $\delta_{2000} = -21^\circ29'29''.7$ are shown in Figure 12.

In Figure 17, we show azimuthal variations across the northern ring. The $\text{H}\alpha$ and IR emission is concentrated to the northwest and northeast. In contrast, the total and flat-spectrum radio emission is brightest directly north. The X-ray emission is a hybrid between these two. The steep-spectrum radio emission exhibits similar azimuthal dependence to the $\text{H}\alpha$ and IR emission in the north but at a smaller radius ($50'' - 80''$).

6. Discussion

Our long-term goal is to understand the origins, evolution, and coupling between the multiple plasmas that exist in Kepler’s SNR. In the current work, we have used radio, X-ray, $H\alpha$, and IR images at a resolution of $7''2$ to compare the signatures of these plasmas in the various wavelength regimes, along with the radio spectral index and polarization measurements. At present, it is not possible to produce a single, coherent picture of the remnant’s complex structures. In this discussion, we identify when clear relationships exist among the multiwavelength structures, and when no single pattern emerges. We explore how the multiple radiative signatures can be used as diagnostics for a variety of underlying physical conditions and processes in Kepler’s SNR, as a step towards the long-term goal.

One example of a clear pattern is the similarity of the $H\alpha$ and IR emission as shown in Figure 12. Although the $H\alpha$ emission results from mostly radiative processes in the northwest and mostly nonradiative processes elsewhere (Fesen *et al.* 1989; Blair *et al.* 1991), there is $12\ \mu\text{m}$ thermal dust emission associated with both types of $H\alpha$ emission processes. The position of the $H\alpha$ emission in front of the X-ray and radio emission is consistent with a circumstellar origin. This is because the lifetime of a neutral atom that has passed through a shock front is short so any emission from the excitation of a neutral atom before it has been ionized by collisions with electrons in the postshock flow must occur immediately behind the shock (Chevalier *et al.* 1980). If the optical (including $H\alpha$) knots are circumstellar in origin then, Douvion *et al.* (1999, 2001) conclude, based on the association of $H\alpha$ and IR emission, that the $12\ \mu\text{m}$ IR emission must also be circumstellar or interstellar in origin.

There are a number of factors which affect the local dynamics of the remnant and would prevent a single global set of relationships between the multiple observed wavelengths. These include variations in external density over a variety of different scales, motion of the progenitor, and asymmetries in the explosion. These will affect the relative strengths and location of the forward and reverse shocks, any bow shock features from the progenitor motion, and the details of the relativistic particle acceleration. Instead of focusing on single, global patterns, we need to examine relationships in different locations of the remnant.

We start by looking directly north where the radio emission is brightest as shown in the grey-scale images of Figures 1, 2, and 12 and the azimuthal profile of Figure 17. The two ways to enhance the synchrotron emission are to amplify the magnetic fields and to increase the number of synchrotron radiating electrons. The radio emission, then, is a measure of the combination of magnetic field strength, thermal density (because the thermal electrons should provide the seed electrons which are accelerated by shocks to relativistic speeds), and the efficiency of the acceleration process. However, Figure 17 shows that the thermal tracers, the $H\alpha$, IR, and X-ray emission, are all weaker directly north where the radio emission is

brightest. If the brightest radio regions are not areas of enhanced density, then either the magnetic fields must be stronger where the radio is brightest or the acceleration process is more efficient.

Comparing the X-ray to the steep and flat spectral components of the radio emission reveals an interesting correlation. As shown in Figure 16, in the southern portion of the ring, the X-ray clearly tracks the steep-spectrum radio emission. In the north to northeast, the X-ray, flat-spectrum radio, and steep-spectrum radio have coincident leading edges. In the northwest, the X-ray more closely tracks the flat-spectrum radio emission. In all cases, the flat-spectrum radio emission either has the same leading edge as or is in front of the steep-spectrum radio emission. Although the radial profiles do not allow us to cleanly separate the flat- and steep-spectrum radio emission, we suggest that the spectral components are superposed along the line of sight. The alternative, that the regions actually represent an intermediate spectral index population, cannot be ruled out using spectral tomography. Figure 17 shows that the X-ray, $H\alpha$, IR, and steep-spectrum radio emission have similar azimuthal profiles over $\approx 150^\circ$ in angle, and are therefore all likely responding to variations in the circumstellar density.

The difference in structure between the flat- and steep-spectrum radio emission suggests that we may be seeing a partial decoupling of the forward and reverse shocks. Because the X-rays in the ROSAT image are mostly line emission from iron and silicon (Kinugasa & Tsunemi 1999), they must be from shocked ejecta rather than shocked ISM. The conditions (such as different temperatures and differing seed particle energy distribution) in the shocked ejecta may produce steeper synchrotron emission than the shocked ISM. One problem here is that the northern ring should be more dense than the southern ring. In this case, a reverse shock should have formed earlier in the north and there should be a greater separation between forward and reverse shocks there than in the south. This is opposite to the observations shown in Figure 16. However, if the forward shock has only very recently encountered denser ISM, its expansion would be slowed, allowing for less separation between the forward and reverse shocks.

Bandiera (1987) proposed a model for the morphology of Kepler’s SNR where the progenitor was a massive runaway star. In this model, a bow shock forms in the direction of motion of the star (to the north). The bow-shocked shell is reshocked by the forward shock and the north-south brightness asymmetry is a direct result of greater density in the north than in the south. Numerical simulations (Borkowski *et al.* 1992) show that there is minimal separation between the bow-shocked shell and the reverse shock in the north. To the south, the bow-shocked shell is less dense and thus less bright than in the north. In this interpretation, the forward shock is not seen because it is now propagating into very low

density ISM. The material in the bow-shocked shell has a higher density and lower temperature than the stellar ejecta. These conditions result in a higher Mach number (and thus a flatter spectral index) for a shock propagating through the bow-shocked material rather than the stellar ejecta. We therefore, still associate the steep-spectrum radio emission with reverse-shocked material, however, the flat-spectrum radio emission is now associated with bow-shocked material.

We now explore why the flat-spectrum radio component, which we suggest indicates the location of either the outer shock or the progenitor bow shock, does not show the same azimuthal structure as the thermal emission shows. Perhaps the anticorrelation seen in Figure 17 is due to a relative weakening of the particle acceleration at the forward shock when regions of high neutral density are encountered. Ion-neutral friction in the upstream flow can damp Alfvén wave growth (Drury *et al.* 1996). Alfvén waves are necessary in the upstream flow to stop particles which have crossed the shock from escaping and reflect them back across the shock allowing the first order Fermi acceleration process to work. Equation 46 from Drury *et al.* (1996) sets the upper cutoff energy for ions and electrons to be reflected by Alfvén waves:

$$\frac{E}{1 \text{ TeV}} < \left(\frac{U}{10^3 \text{ km s}^{-1}} \right)^3 \left(\frac{T}{10^4 \text{ K}} \right)^{-0.4} \\ \times \left(\frac{n_n}{1 \text{ cm}^{-3}} \right)^{-1} \left(\frac{n_i}{1 \text{ cm}^{-3}} \right)^{0.5} \left(\frac{\mathcal{P}_0}{0.1} \right).$$

Here, U is the shock velocity, T is the preshock temperature, n_n is the neutral number density, n_i is the ion number density, and \mathcal{P}_0 is the dimensionless resonant cosmic ray pressure at the shock. Any particles with energies higher than E will escape upstream. To determine the upper cutoff energy, we first take $n_n = 7 \text{ cm}^{-3}$ and $U = 1500 \text{ km s}^{-1}$ from Blair *et al.* (1991). We then assume, for 600 pc above the galactic plane, that $T = 10^4 \text{ K}$ and $n_i = 1 \text{ cm}^{-3}$ (an ionization fraction of 13 %). Then, if the shock acceleration is efficient ($\mathcal{P}_0 = 0.1$), the upper cutoff energy is 480 GeV.

The above cutoff energy is too high to affect our radio measurements. Suppose, however, the shock acceleration is less efficient than assumed above, leading to a smaller \mathcal{P}_0 . A lower limit to the resonant cosmic ray pressure can be set by the presence of background cosmic rays which have an energy density of $\approx 1 \text{ eV cm}^{-3}$. Dividing the background cosmic ray pressure by the ram pressure of upstream ions results in a dimensionless pressure of 4.7×10^{-5} . Using this pressure, the upper energy cutoff now becomes 0.2 GeV. The electrons radiating at 6 cm have energies of 4 GeV, if the magnetic field and particle energies are in equipartition. Therefore, it is possible that Alfvén wave damping is occurring to some degree in Kepler’s SNR and this results in the anticorrelation of the flat-spectrum radio emission and the

thermal emission. It would be useful to explore the possible contribution of Alfvén wave damping for spectral variations in other SNRs.

We now turn to the structural aspects of the remnant and the connection with underlying dynamics. There are two primary classes of radio structure in the remnant as identified from the tomography images shown in Figure 7 and labelled in Figure 2. The ring, consisting of the structures labelled as the northern ring and southern ring, is a composite of both flat and steep spectral components. The non-ring features include the ears, central band, bump, steep arc, and western stub. The non-ring features are all steep in spectral index which leads one to ask if they are spatially connected with each other and/or with the steep parts of the ring. Unfortunately, there does not seem to be an easy way to connect these features into a coherent structure. This lack of connection is also evident in the rotation measure image of Figure 10 that does not show the same structures as the spectral index image. We might expect spatially coherent structures to show a clear pattern in rotation measure, but none is apparent.

The ears, labelled in Figure 2, may arise due to expansion into a lower density medium. Pressure equilibrium in the presupernova ISM leads to higher temperatures in lower density areas. Higher temperatures result in higher sound speeds and thus lower Mach numbers in these regions if the shock velocity is independent of density. Lower Mach numbers indicate weaker shocks and thus steeper expected spectral indices. To see if this hypothesis is plausible, consider the relation between spectral index and Mach number for first-order Fermi acceleration in the test particle limit, $\alpha = (M^2 + 3)/2(M^2 - 1)$. If $\alpha = 0.65(0.8)$, then $M = 3.8(2.8)$. The resulting density ratio between a flat spectral region in the north and a steep spectral region in the western ear is $n_f/n_s = (M_f/M_s)^2 = 1.8$ which is certainly within reason.

The fact that the ears are 180° apart indicates that, if the progenitor was really a massive star, the stellar wind may have been axisymmetric (Blondin *et al.* 1996). This model predicts the shapes of very young SNRs and might be extendable to Kepler’s higher age. However, if the progenitor was a runaway star, as suggested by Bandiera (1987), then the axisymmetry would be lost. There is evidence, however, that the progenitor’s stellar wind has modified the circumstellar environment at the current shell radius because the optical knots are thought to be material ejected by that wind (Blair *et al.* 1991).

An alternative source of the ear structures could be a strongly magnetized interstellar medium (Insertis & Rees 1991; Różyczka & Tenorio-Tagle 1995). An SNR evolving in such a medium will become elongated along the direction of the field. This may also explain the steeper spectral indices in the ears because shocks propagating parallel to the ambient magnetic field produce steeper spectra than shocks propagating perpendicular to the magnetic

field (Fulbright & Reynolds 1990). However, this model cannot explain the almost spherical symmetry of the rest of the remnant and requires a magnetic field much stronger than is thought to exist in the ambient interstellar medium so far from the galactic plane. Finally, the ears could also be due to collimated outflows from a central source as Gaensler *et al.* (1998) suggest for G309.2-00.6. However, no jet-like structure or compact object is identified in Kepler. None of these models for the ears — axisymmetric wind, interstellar magnetic fields, or collimated outflows — explains the significant north-south brightness asymmetry seen in all bands.

The generally radial orientation of the magnetic field shown in Figure 11 is consistent with what we expect from Rayleigh-Taylor (RT) instabilities in the decelerating remnant (Gull 1975; Chevalier 1976) and is common in young SNRs (Milne 1988). The deviations from the radial pattern are explained by Dickel *et al.* (1989) as due to an inhomogeneous circumstellar medium (CSM). Dickel *et al.* (1989) used clump radii of 10^{17} cm which correspond to angular diameters of $2''.7$ at the distance of Kepler which is smaller than our current resolution of $7''.2$. With a clumpy CSM, RT instabilities and MHD turbulence develop at every clump, which can account for both the observed magnetic field patterns and the brightness distribution in the remnant. We might expect to see magnetic field patterns corresponding to brightness variations in the radio, X-ray, $H\alpha$, and IR images shown in Figure 12. No correlation is seen with radio brightness features. No obvious correlation exists with the X-ray, $H\alpha$, and IR brightness either, but severe depolarization limits magnetic field measurements in the highest density regions. If density variations (clumps) are responsible for non-radial magnetic field patterns, we might also expect to see a correspondence with spectral index as shown in Figure 4, but we do not.

7. Conclusions

In this paper we have presented a new epoch of radio spectral and polarization data for Kepler’s SNR. We have also compared our new radio data to $H\alpha$, X-ray, and IR images to better understanding the interactions between the nonthermal and thermal plasmas. We identify the following primary results:

1. There is a general north-south asymmetry in all emission and polarization measures.
2. For the first time spatial spectral index variations are observed between 6 cm and 20 cm in Kepler’s SNR. The spectral indices range from -0.85 to -0.6 with a mean of -0.71 .
3. The mean percent polarization is 3.5% at 20 cm and 6% at 6 cm.

4. Although there are interesting small-scale features such as the bump and the western ear, there is no clear large-scale pattern between spectrally steep features and rotation measure, depolarization, or thermal emission.
5. There are several strong correspondences between the radial and azimuthal profiles of the radio, X-ray, $H\alpha$, and IR emission in different parts of the remnant although there is no single, global pattern.
6. The striking similarity between the $H\alpha$ and IR images suggests that the $12\ \mu\text{m}$ thermal dust emission must have the same origin as the optical emission, namely shock heating of the CSM/ISM.
7. The brightest thermal emission regions correspond to the strongest radio depolarization indicating that the thermal and nonthermal plasmas are mixed.
8. The flat-spectrum and steep-spectrum radio emission indicate forward- and reverse-shocked material, respectively, and indicate a partial decoupling of these shocks in the southern portion of the remnant.
9. The flat-spectrum radio emission may alternatively indicate bow-shocked material (reshocked by the forward shock) from the progenitor's motion through the ISM.
10. The anticorrelation in the azimuthal profiles of the flat-spectrum radio emission and the thermal emissions may indicate that Alfvén wave damping is occurring to some degree in Kepler's SNR.
11. The ears may result from expansion into a lower density medium and any model used to explain the ears must include axisymmetry.
12. The magnetic field is generally radial as expected, but small-scale magnetic field patterns do not correspond to brightness variations in the radio, X-ray, $H\alpha$, or IR. There is also no correlation between magnetic field patterns and radio spectral index.

To date there are still many unresolved issues about how the thermal and nonthermal plasmas are coupled in SNRs. Many different correlations between measures exist, but often no clear pattern emerges. Comparison with proper motion measurements is essential to help define why certain correlations exist in certain cases. Future observations must also be conducted with *Chandra* and SIRTf which will provide higher spatial resolution and allow us to more definitively determine the relationships between the thermal and nonthermal plasmas.

This work has been conducted with support by NSF grant AST 96-19438 at the University of Minnesota. We wish to thank P.-O. Lagage and T. Douvion for providing an IR image, W. Blair for the H α image, and the ROSAT public archive for the X-ray data. We also wish to thank Udo Gieseler and Tom Jones for valuable conversations. We acknowledge the use of NASA's *SkyView* facility ⁴ located at NASA Goddard Space Flight Center for providing the DSS and 2MASS images which were used to register the H α and IR images. We finally wish to thank the referee for many valuable comments.

REFERENCES

- Anderson, M. C. & Rudnick, L. 1993, ApJ, 408, 514
- Anderson, M. C. & Rudnick, L. 1996, ApJ, 456, 234
- Anderson, M. C., Rudnick, L., Leppik, P., Perley, R., & Braun, R. 1991, ApJ, 373, 146
- Baade, W. 1943, ApJ, 97, 119
- Bandiera, R. 1987, ApJ, 319, 885
- Bandiera, R. & van den Bergh, S. 1991, ApJ, 374, 186
- Blair, W. P., Long, K. S., & Vancura, O. 1991, ApJ, 366, 484
- Blondin, J. M., Lundqvist, P., & Chevalier, R. A. 1996, ApJ, 472, 257
- Borkowski, K. J., Blondin, J. M., & Sarazin, C. L. 1992, ApJ, 400, 222
- Braun, R. 1987, A&A, 171, 233
- Brotten, N. W., MacLeod, J. M., & Vallée, J. P. 1988, Ap&SS, 141, 303
- Chevalier, R. A. 1976, ApJ, 207, 872
- Chevalier, R. A., Kirshner, R. P., & Raymond, J. C. 1980, ApJ, 235, 186
- Dennefeld, M. 1982, A&A, 112, 215
- Dickel, J. R., Eilek, J. A., Jones, E. M., & Reynolds, S. P. 1989, ApJS, 70, 497
- Dickel, J. R., Sault, R., Arendt, R. G., Matsui, Y., & Korista, K. T. 1988, ApJ, 330, 254

⁴<http://skyview.gsfc.nasa.gov>

- D'Odorico, S., Bandiera, R., Danziger, J., & Focardi, P. 1986, *AJ*, 91, 1382
- Douvion, T., Lagage, P. O., Ballet, J., Boulanger, F., Cesarsky, C. J., Cesarsky, D., & Claret, A. 1999, in *The Universe as seen by ISO: ESA proceedings SP-427*, ed. P. Cox & M. F. Kessler, (ESTEC, Noordwijk, The Netherlands: ESA Publications Division), 301
- Douvion, T., Lagage, P. O., Cesarsky, C. J., & Dwek, E. 2001, *A&A*, 373, 281
- Draine, B. 1981, *ApJ*, 245, 393
- Drury, L. O'C, Duffy, P., & Kirk, J. G. 1996, *A&A*, 309, 1002
- Fesen, R. A., Becker, R. H., Blair, W. P., & Long, K. S. 1989, *ApJ*, 338, L13
- Fulbright, M. S. & Reynolds, S. P. 1990, *ApJ*, 357, 591
- Gaensler, B. M., Green, A. J., & Manchester, R. N. 1998, *MNRAS*, 299, 812
- Gull, S. F. 1973, *MNRAS*, 161, 47
- Gull, S. F. 1975, *MNRAS*, 171, 263
- Hughes, J. P. 1999, *ApJ*, 527, 298
- Hughes, J. P. 2000, *ApJ*, 545, L53
- Insertis, F. M. & Rees, M. J. 1991, *MNRAS*, 252, 82
- Jones, T. W., *et al.* 1998, *PASP*, 110, 125
- Katz-Stone, D. M., Kassim, N. E., Lazio, T. J. W., & O'Donnell, R. 2000, *ApJ*, 529, 453
- Katz-Stone, D. M. & Rudnick, L. 1997, *ApJ*, 488, 146
- Kinugasa, K. & Tsunemi, H. 1999, *PASJ*, 51, 239
- Koralesky, B., Rudnick, L., Gotthelf, E. V., & Keohane, J. W. 1998, *ApJ*, 505, L27
- Matsui, Y., Long, K. S., Dickel, J. R., & Greisen, E. W. 1984, *ApJ*, 287, 295
- Milne, D. K. 1987, *Aust. J. Phys.*, 40, 771
- Milne, D. K. 1988, in *Supernova Remnants and the Interstellar Medium*, ed. R. S. Roger & T. L. Landecker, (Cambridge: Cambridge University Press), 351
- Reynolds, S. P. & Ellison, D. C. 1992, *ApJ*, 399, L75

Reynoso, E. M. & Goss, W. M. 1999, *AJ*, 118, 926

Różyczka, M. & Tenorio-Tagle, G. 1995, *MNRAS*, 274, 1157

Simard-Normandin, M. & Kronberg, P. P. 1980, *ApJ*, 242, 74

Table 1. VLA Observations

Date	Configuration	Wavelength (cm)	Bandwidth (MHz)	On-Source Time per Frequency (minutes)
1997 May	B	20	25	101
		6		362
1997 Jul	C	20	25	43
		6		145
1997 Dec, 1998 Jan	D	20	25	15
		6		77
1998 Mar, Apr	A	20	12.5	83

Table 2. Statistics for Radio Total Intensity Images

Frequency (MHz)	Integrated Flux Density (Jy)	Off Source RMS Noise (mJy bm^{-1})
1285.0	15.4	0.27
1365.1	14.8	0.34
1402.5	14.6	0.39
1464.9	14.2	0.29
4835.1	6.1	0.12
4885.1	6.1	0.15

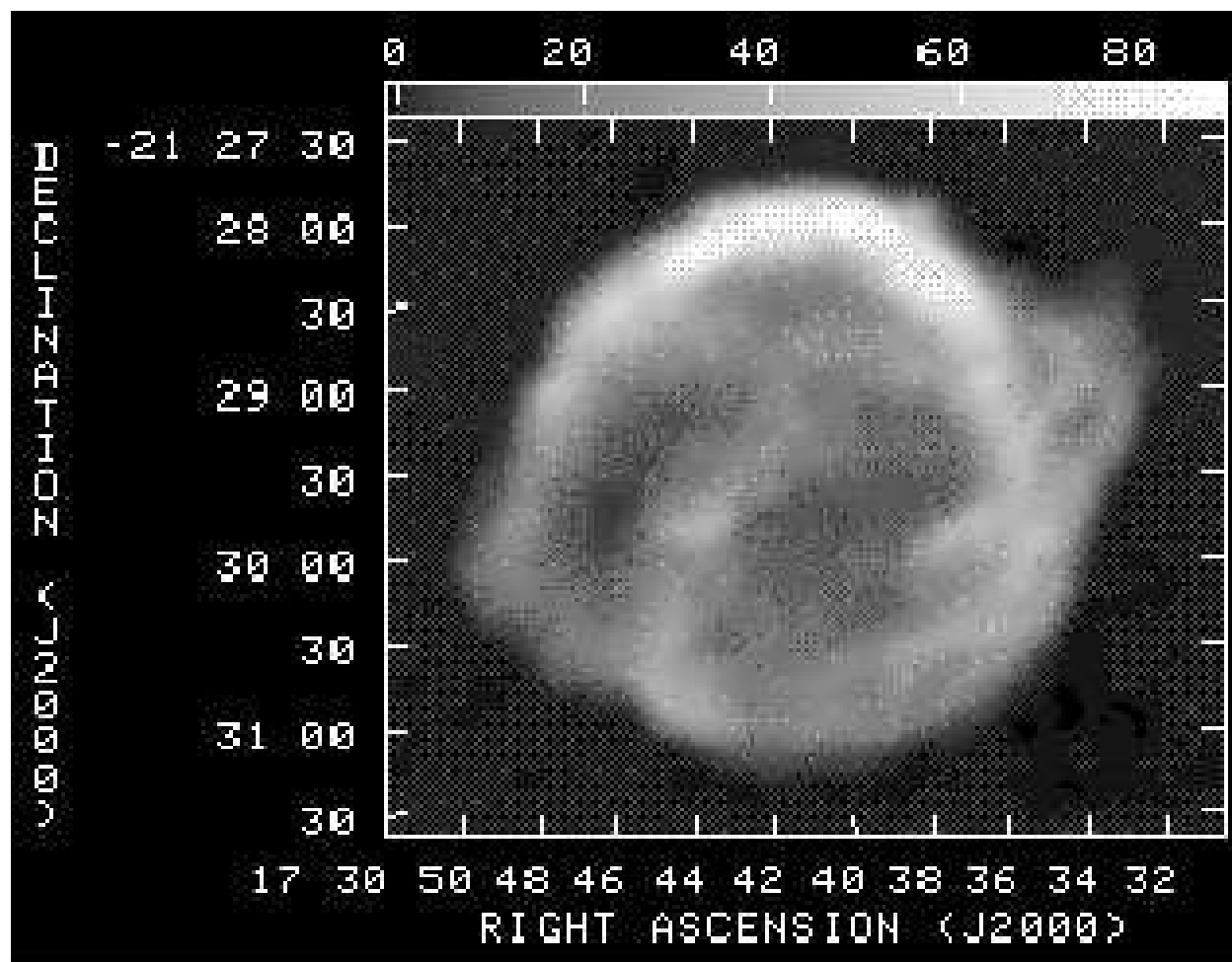


Fig. 1.— Gray-scale image of Kepler's SNR at 20 cm. The resolution is 7".2. The brightness scale is in mJy bm⁻¹.

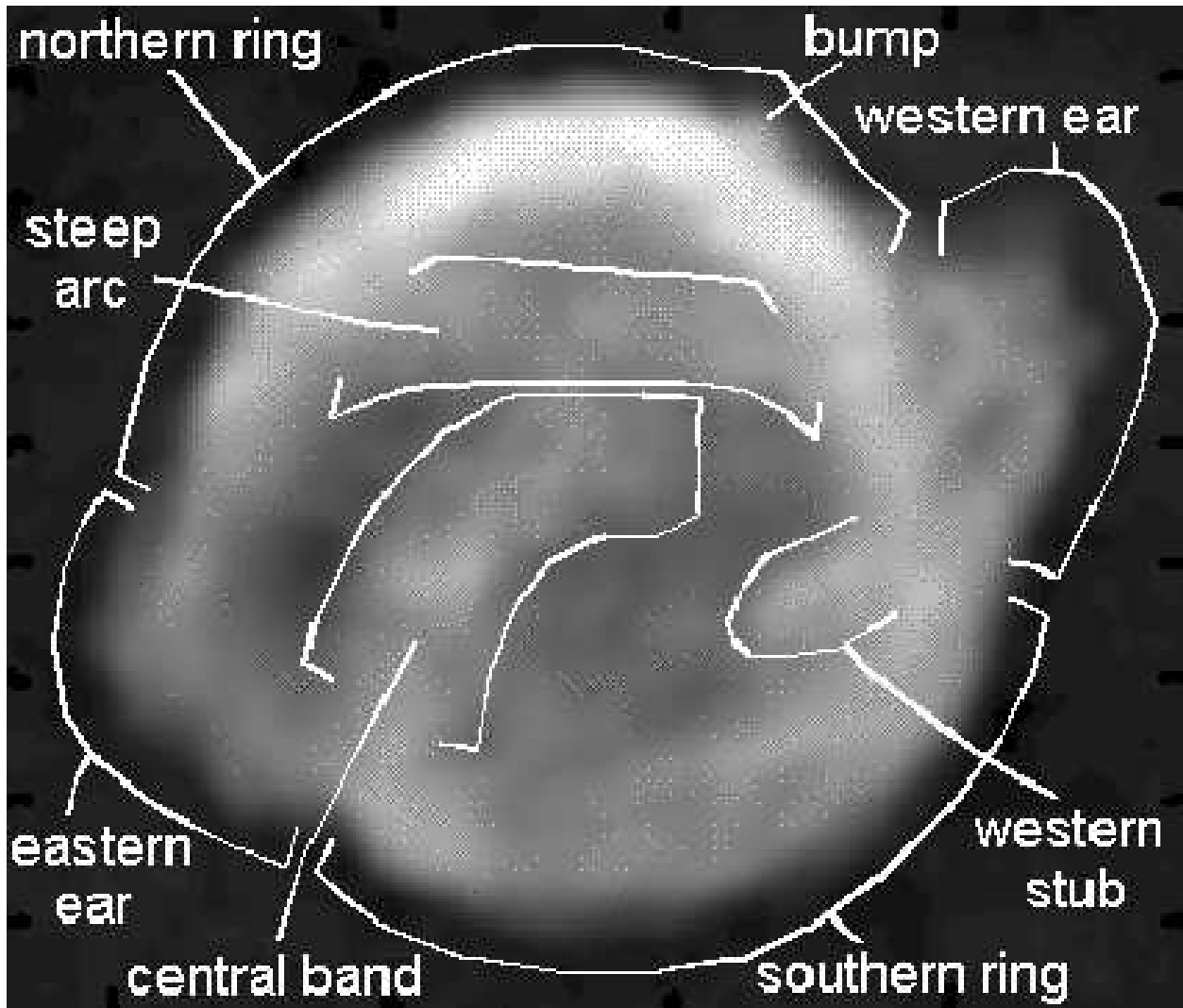


Fig. 2.— Gray-scale image of Kepler's SNR at 6 cm. The resolution is $7''.2$. The gray-scale brightness range is -0.35 to $35.78 \text{ mJy } \text{bm}^{-1}$.

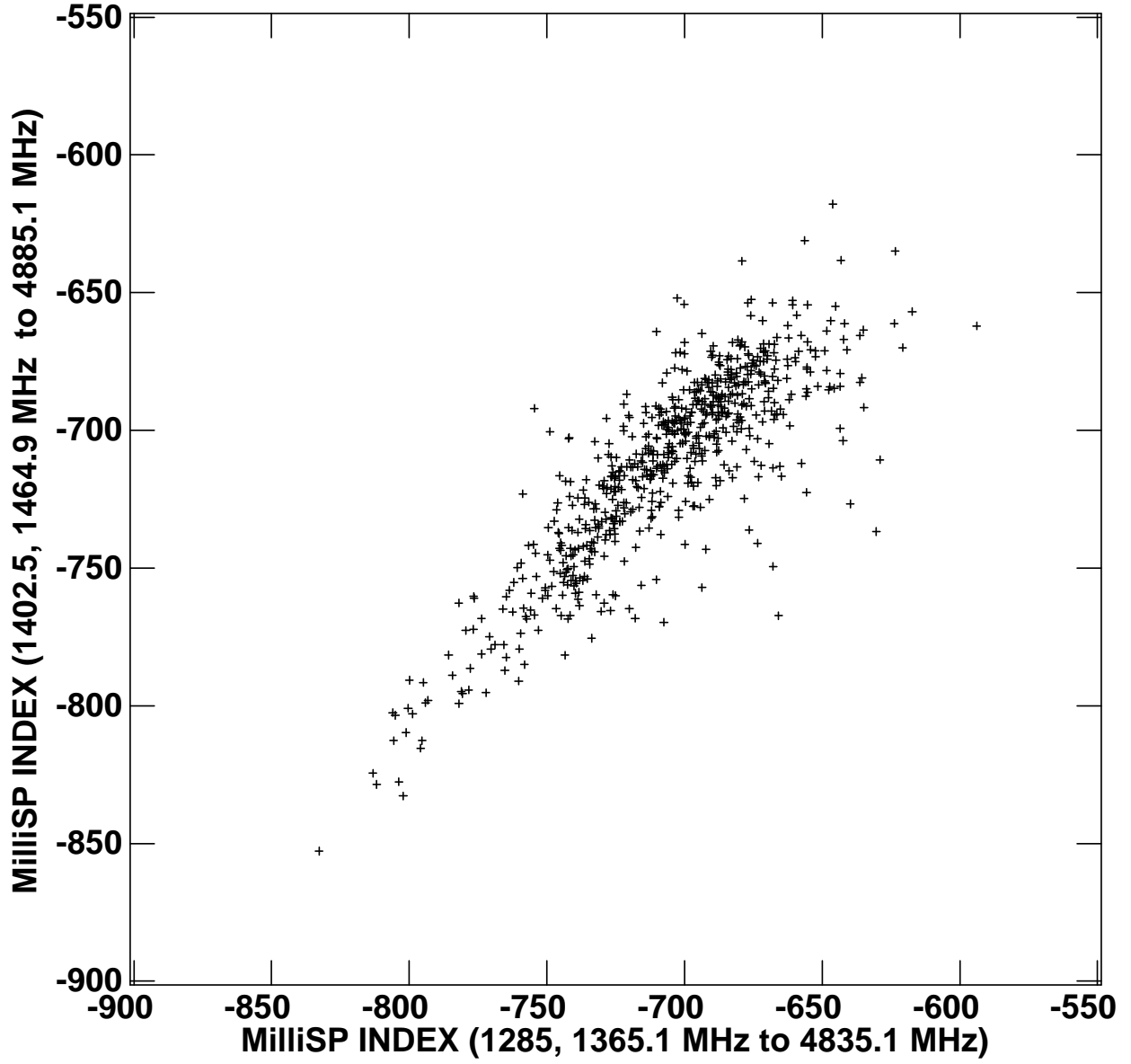


Fig. 3.— Spectral index from pair 2 *vs.* spectral index from pair 1. Points are sampled once per resolution element (beam).

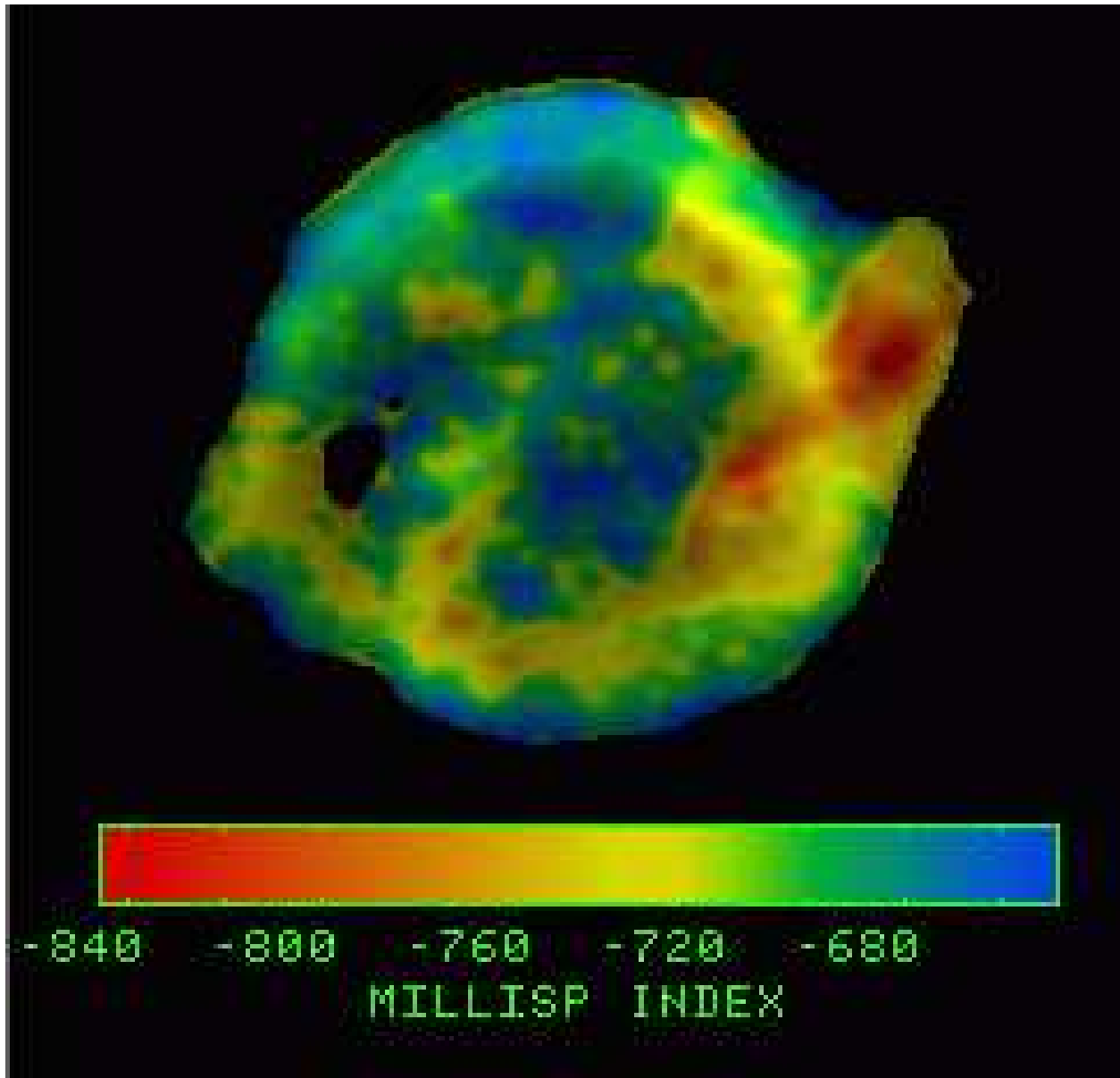


Fig. 4.— Spectral index between 6 cm and 20 cm. Intensity is set by the 6 cm continuum image.

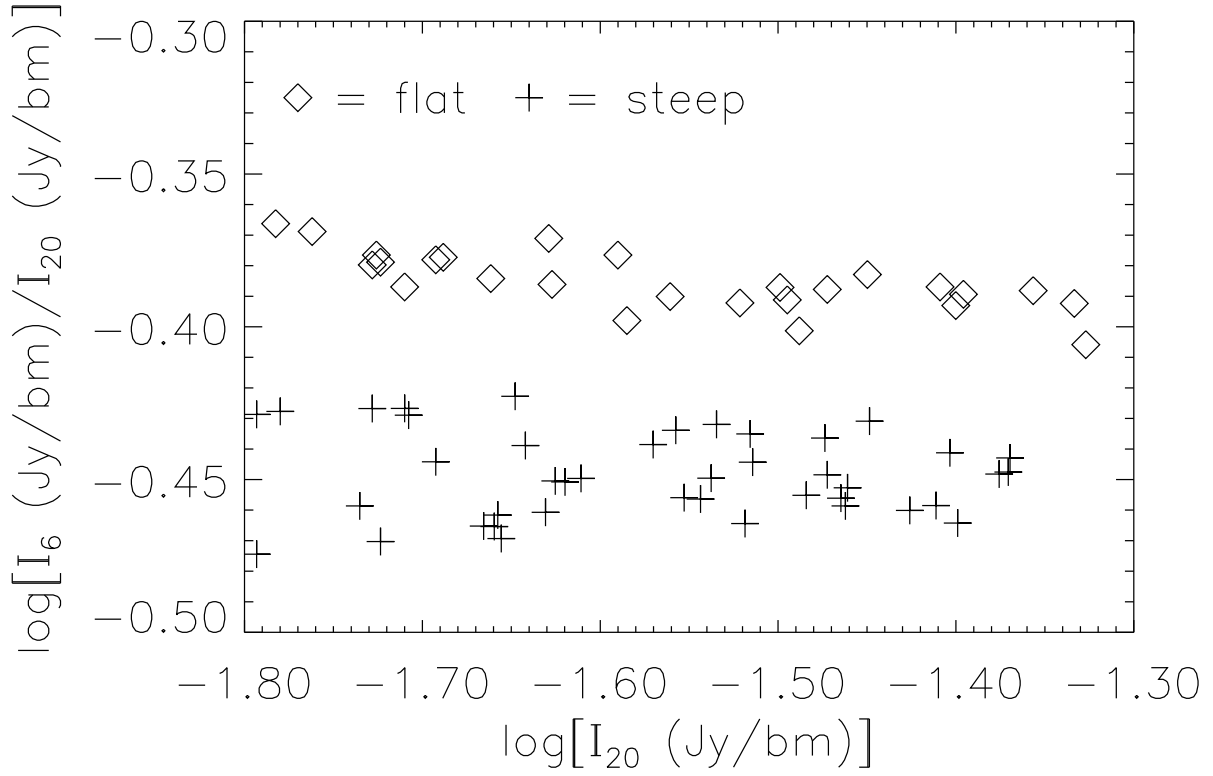


Fig. 5.— $\log(I_6/I_{20})$ vs. $\log(I_{20})$, where I_x is the intensity in band x, for a continuous flat spectral region (diamonds) and a continuous steep spectral region (pluses).

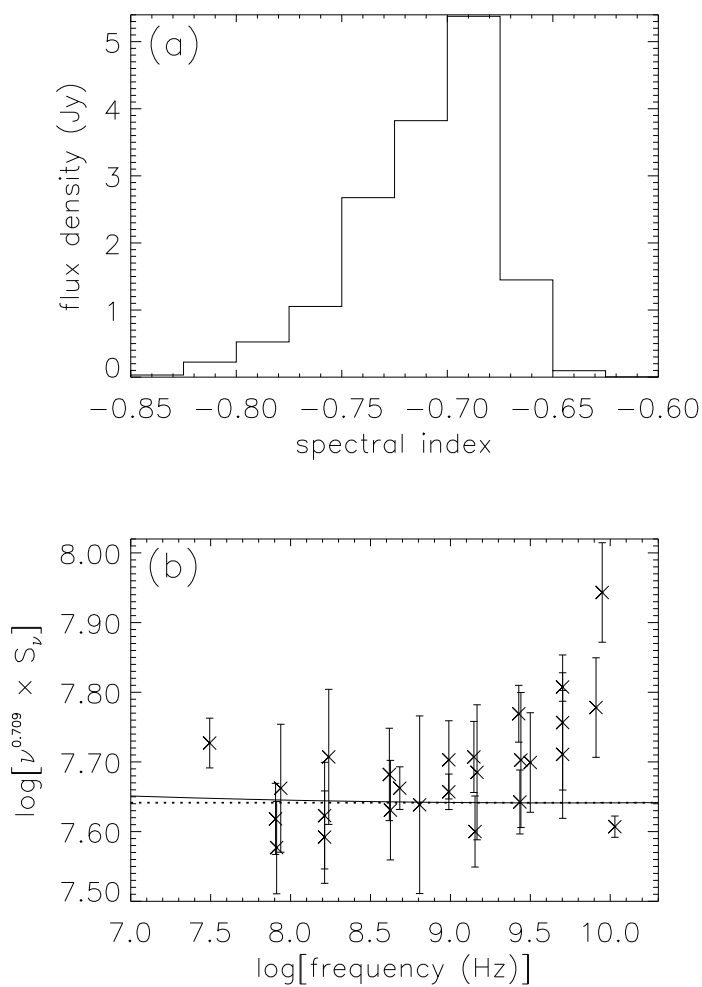


Fig. 6.— (a) The result of binning the observed 20 cm flux densities into 10 spectral index bins. (b) The solid line is the result of adding together the 10 power laws representing each bin. The dotted line represents a power law with an index of -0.709 . The data points with errors are taken from a spectral plot by Reynolds & Ellison (1992).

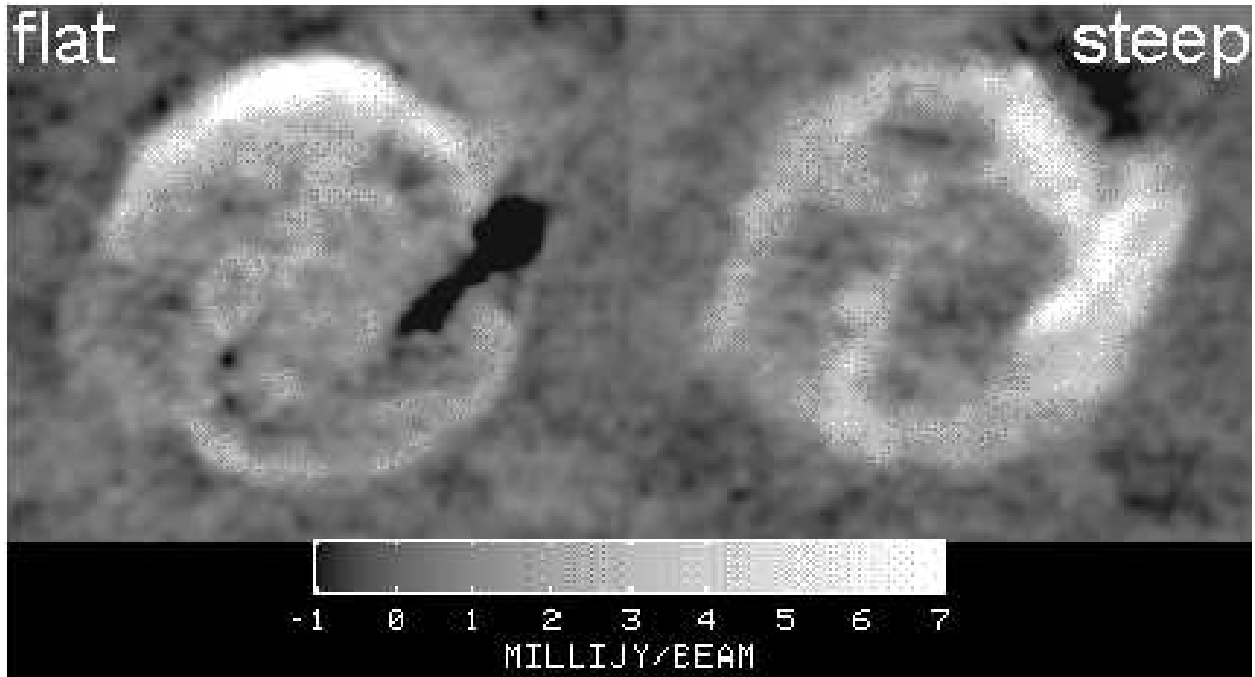


Fig. 7.— Two representative spectral tomography images between 20 cm and 6 cm. On the right, bright areas have radio spectral indices steeper than -0.65 . On the left, the intensity scale is reversed and the zero point shifted so that bright areas have spectral indices flatter than -0.75 and the dark areas steeper indices. The grey-scale for intensity is the same on both images.

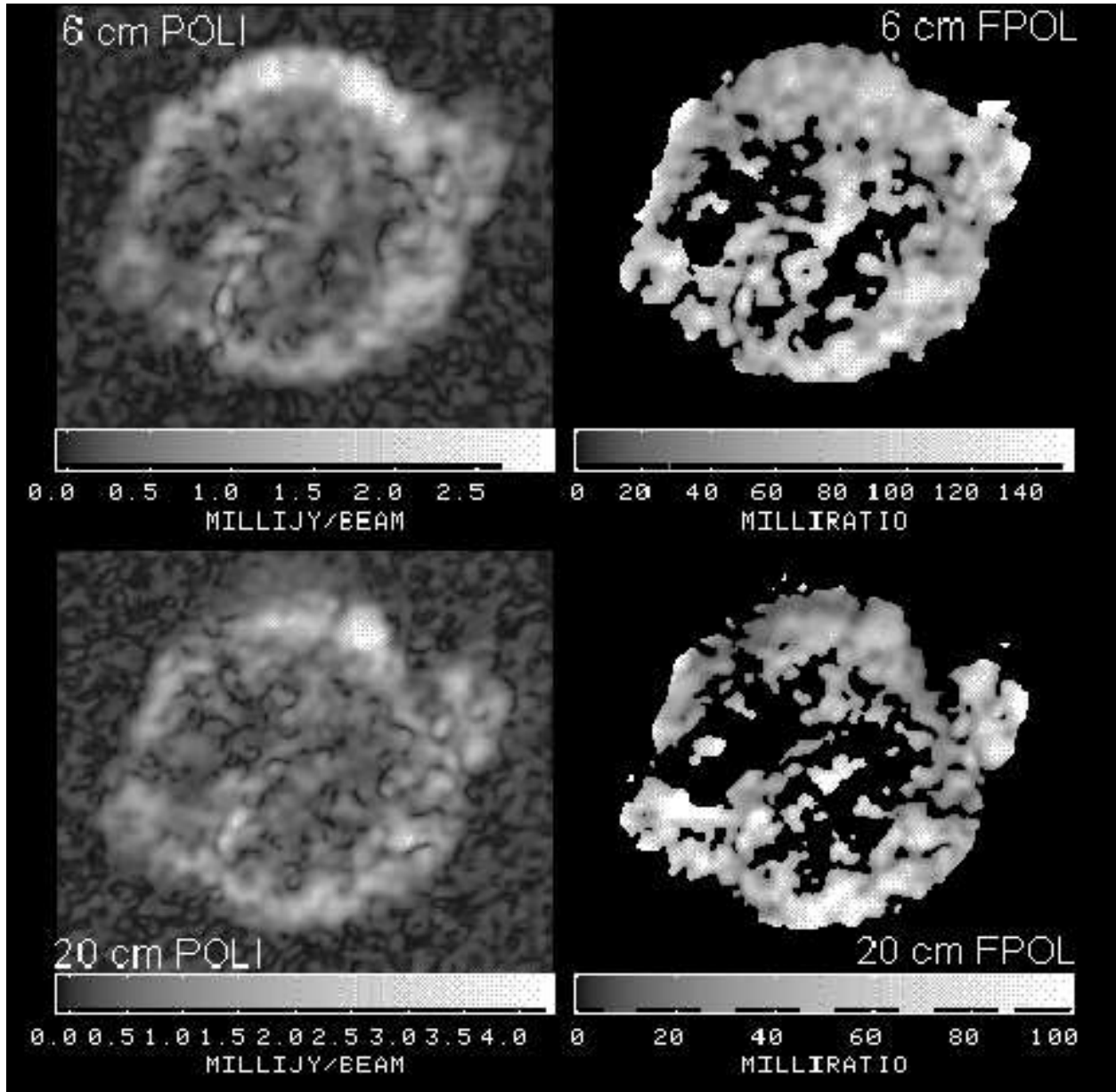


Fig. 8.— Gray-scale images of 6 cm polarized intensity (top left), 6 cm fractional polarization (top right), 20 cm polarized intensity (bottom left), and 20 cm fractional polarization (bottom right).

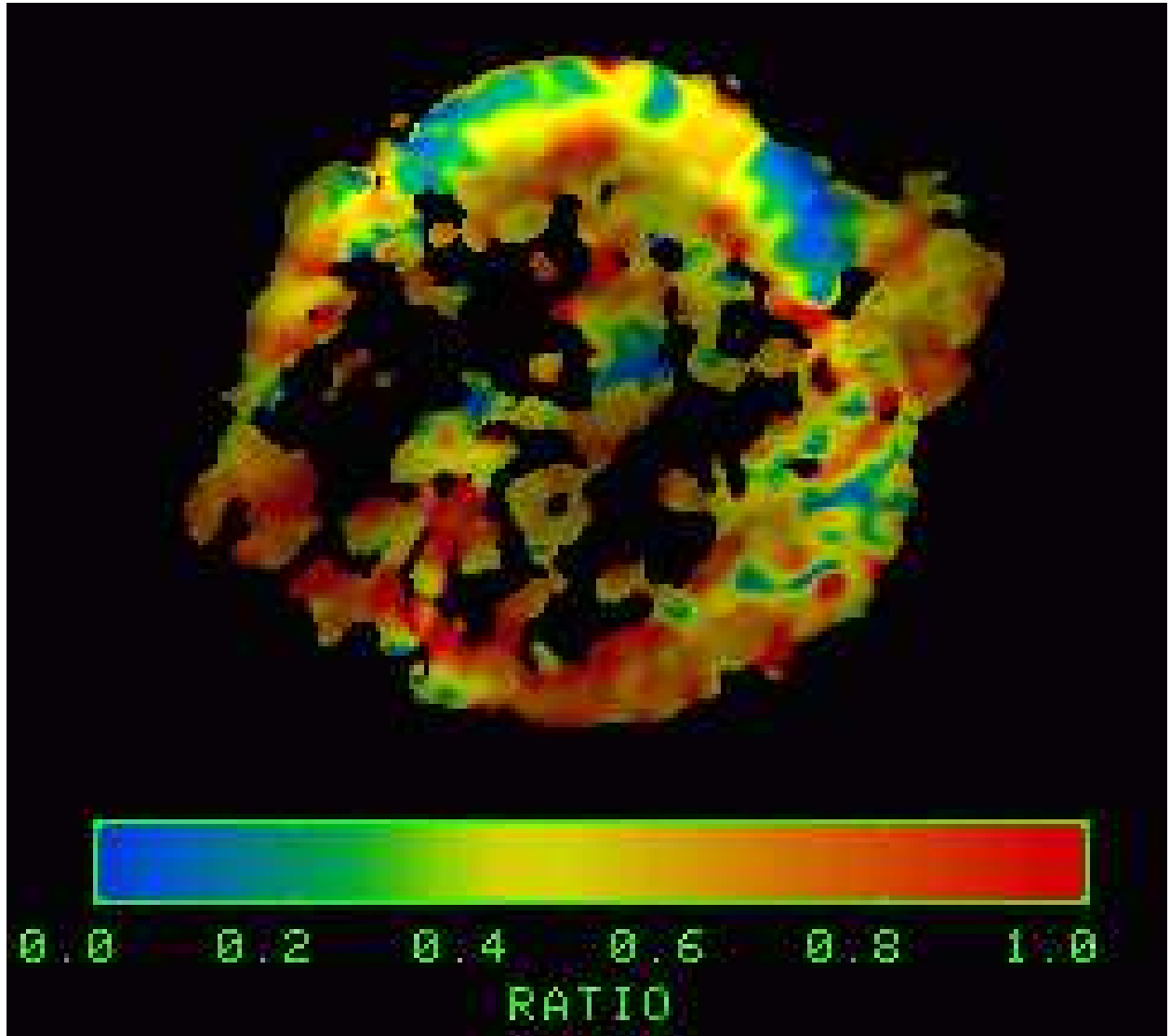


Fig. 9.— Depolarization image from 6 cm to 20 cm as defined in the text. Intensity is set by the 6 cm radio total intensity image.

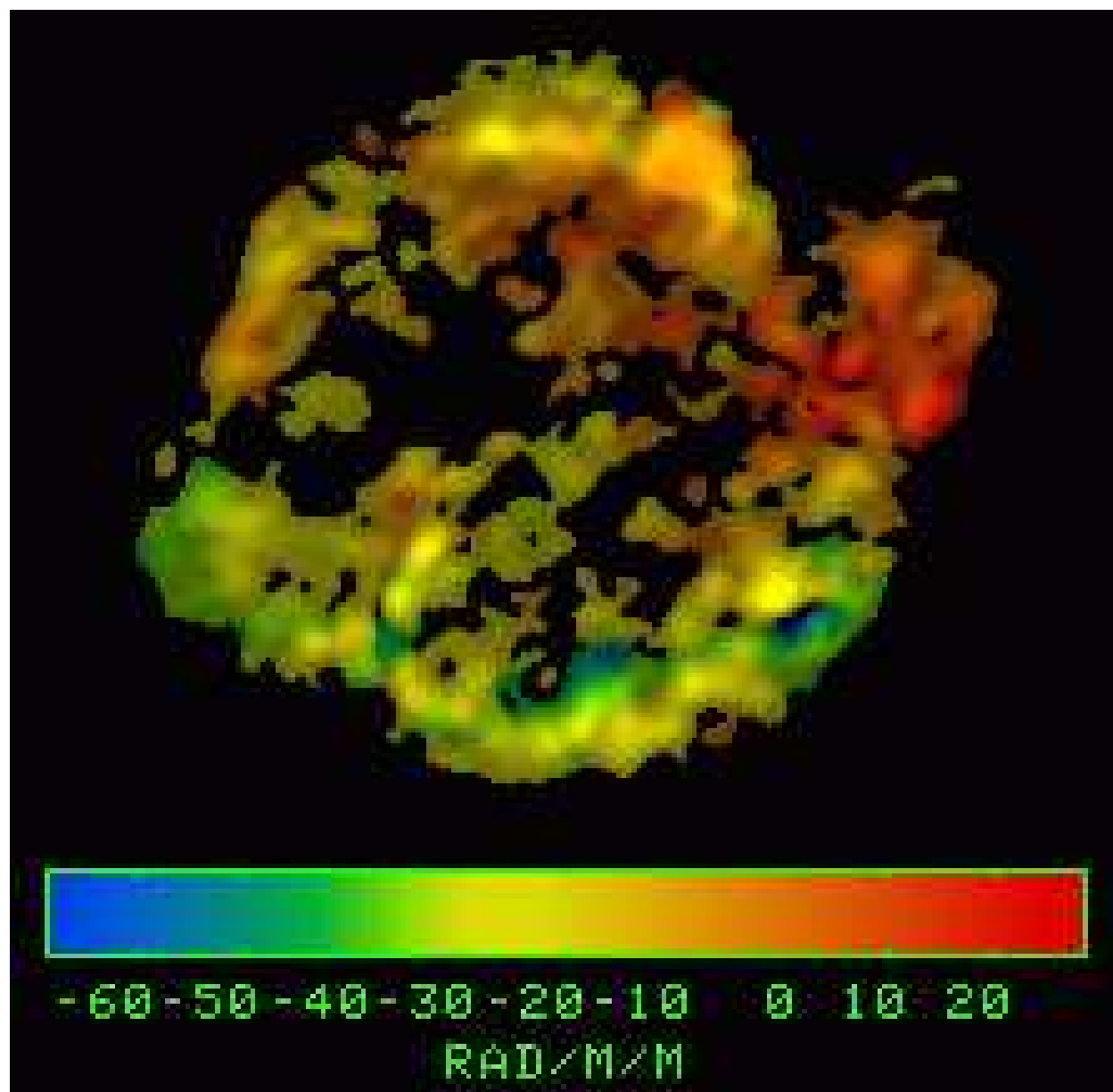


Fig. 10.— Rotation measure between 6 cm and 20 cm. Intensity is set by the 20 cm polarized intensity image.

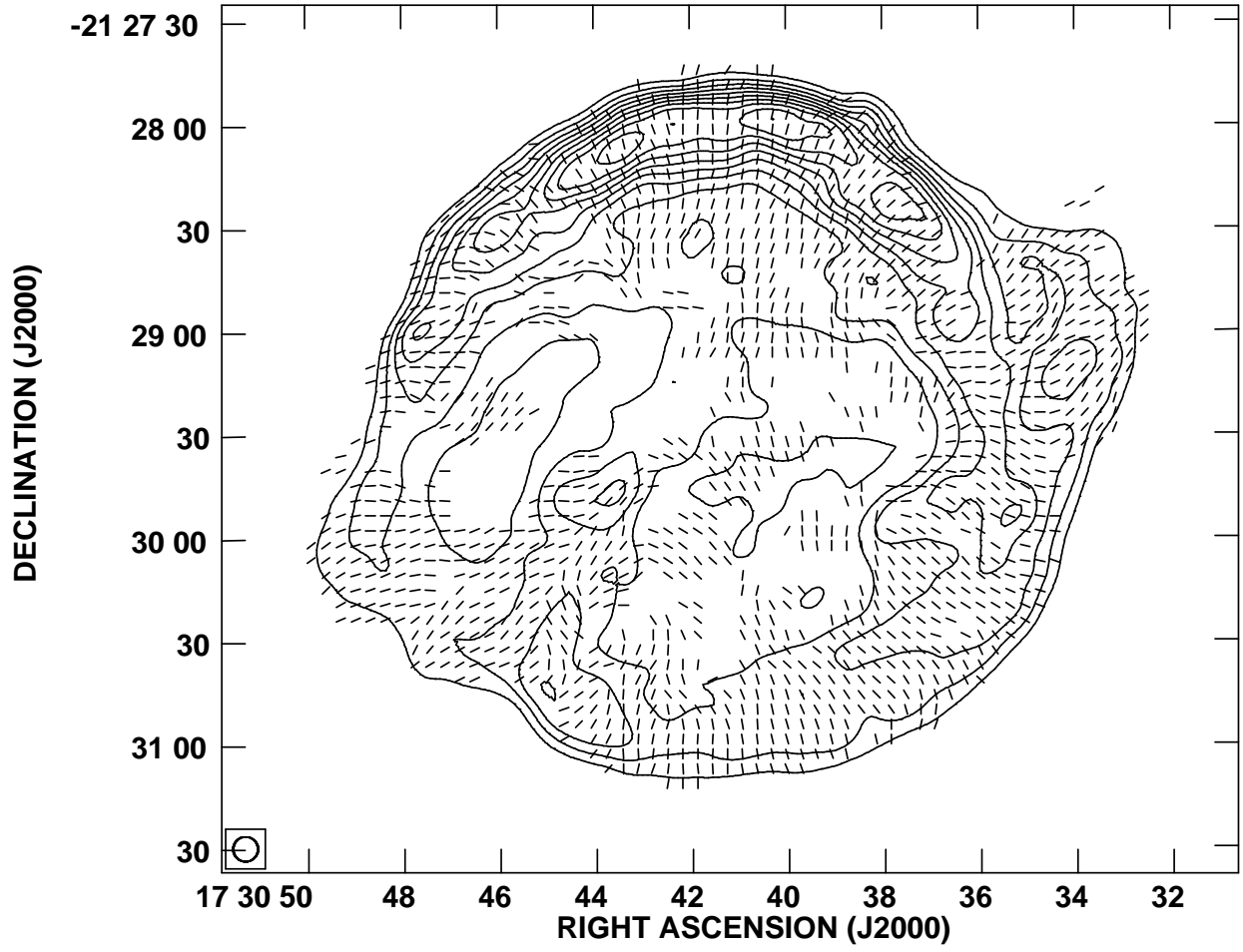


Fig. 11.— The magnetic field structure in Kepler's SNR. All vectors are the same length. The contours are 6 cm total intensity.

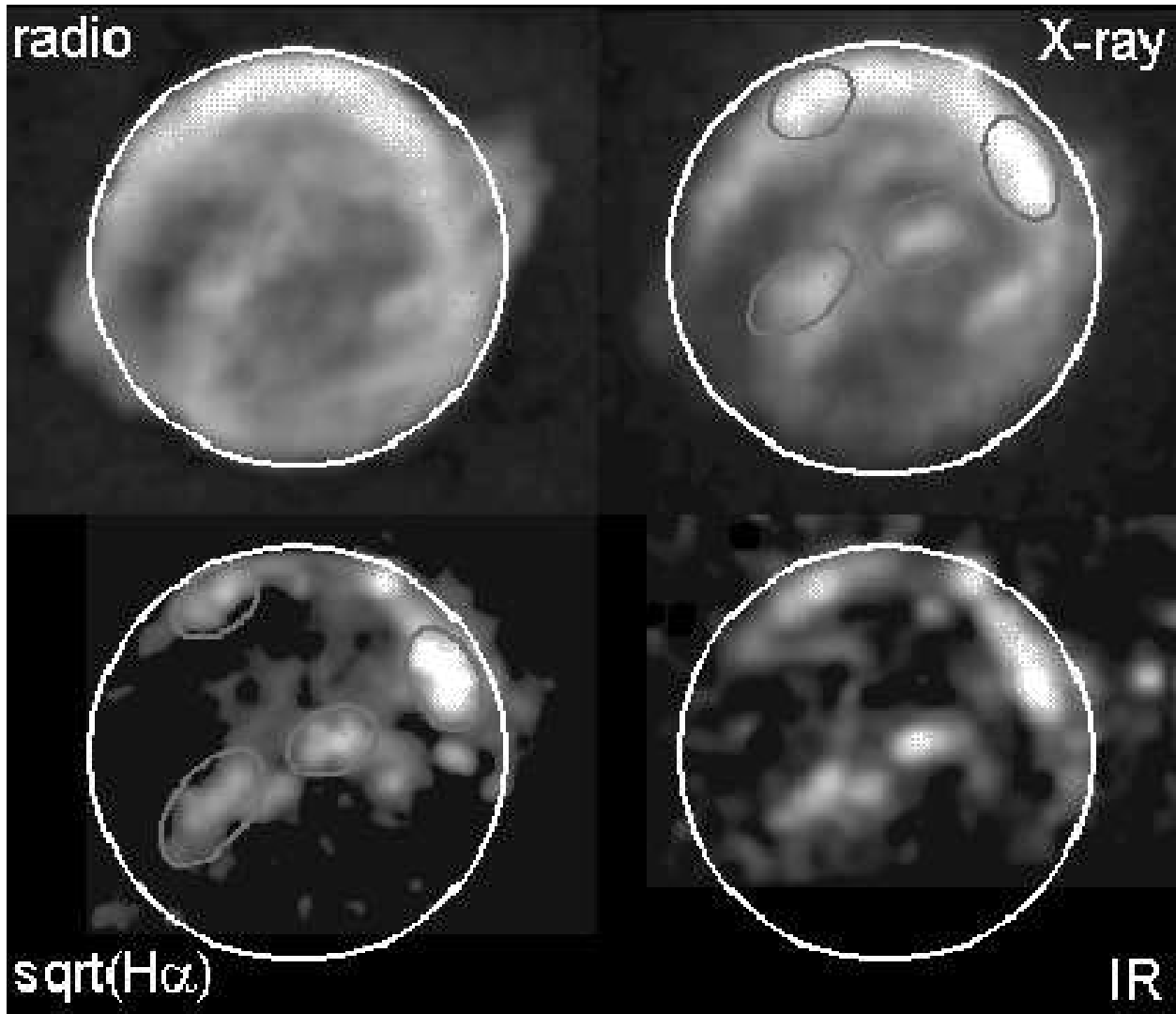


Fig. 12.— Gray-scale images of 6 cm radio continuum (top left), X-ray (top right), $H\alpha$ (bottom left), and IR (bottom right). The circles are $100''$ in radius.

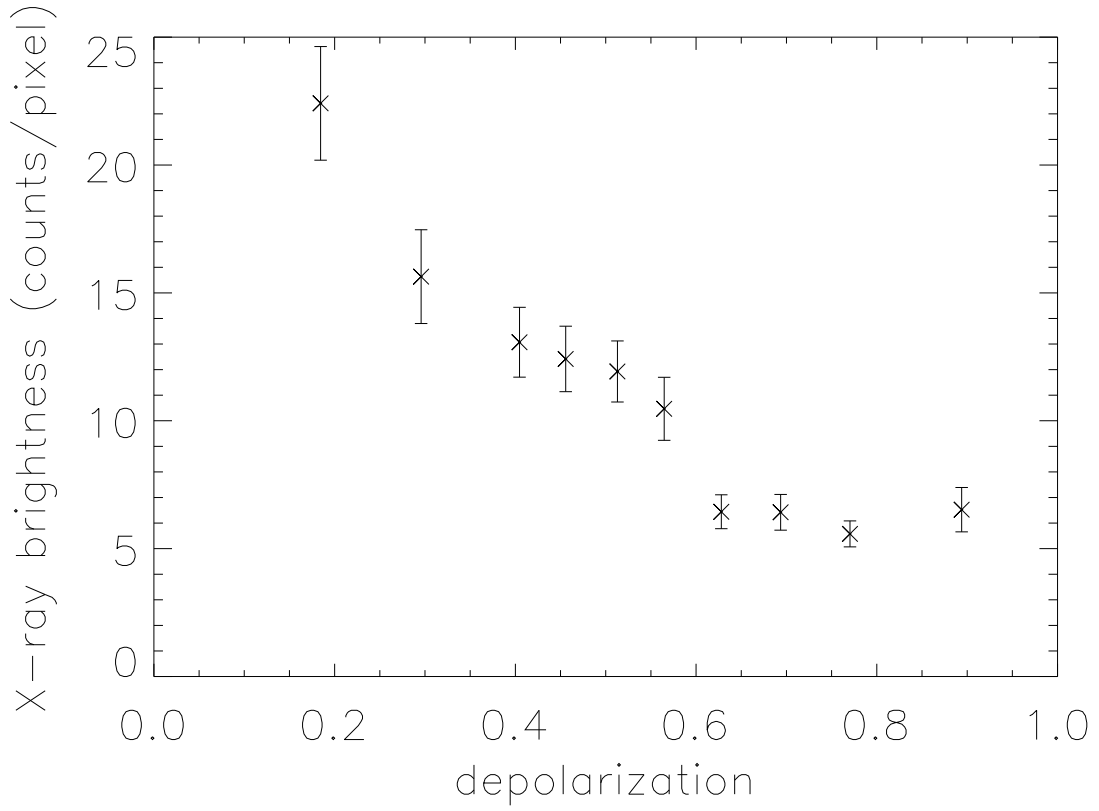


Fig. 13.— Comparison of X-ray brightness *vs.* depolarization. The \times 's represent the mean X-ray brightness in bins which are 45 beam-independent data points wide in depolarization. The error bars represent the rms error in the mean X-ray brightness in each depolarization bin. The rms scatter per independent beam is ≈ 7 times higher in each bin than the errors in the mean.

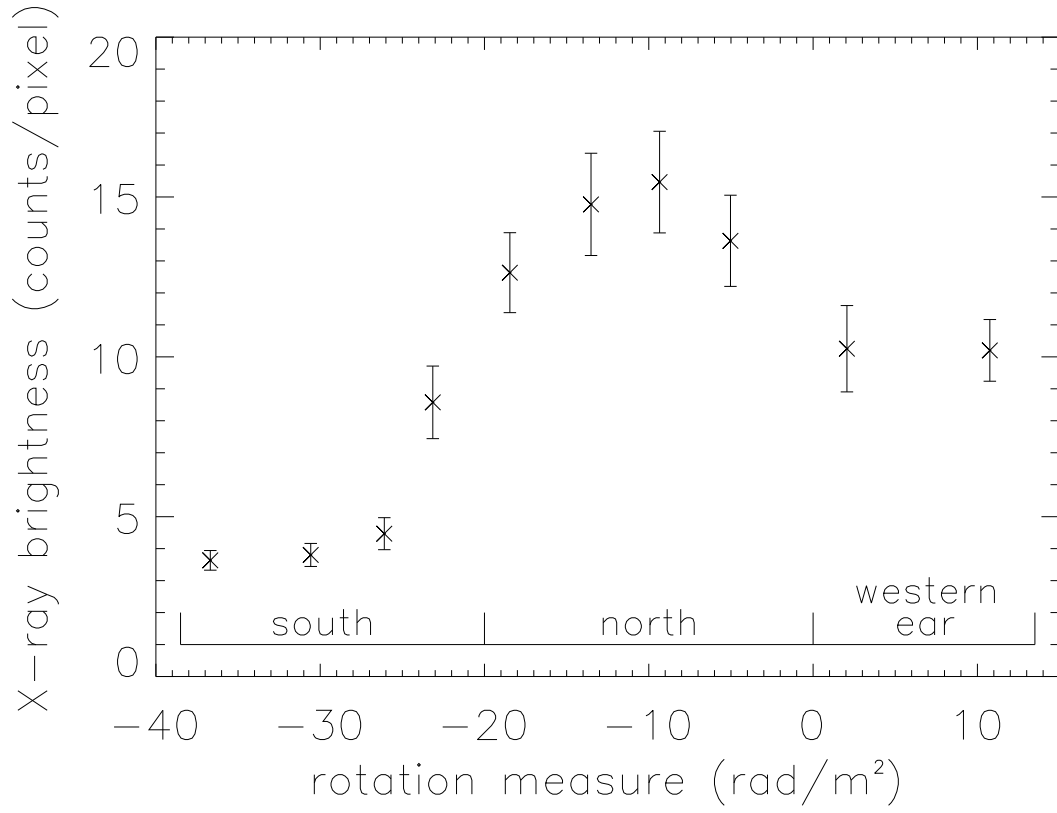


Fig. 14.— Comparison of X-ray brightness *vs.* rotation measure. The \times 's represent the mean X-ray brightness in bins which are 50 beam-independent data points wide in rotation measure. The error bars are set by the rms of the mean X-ray brightness in each bin.

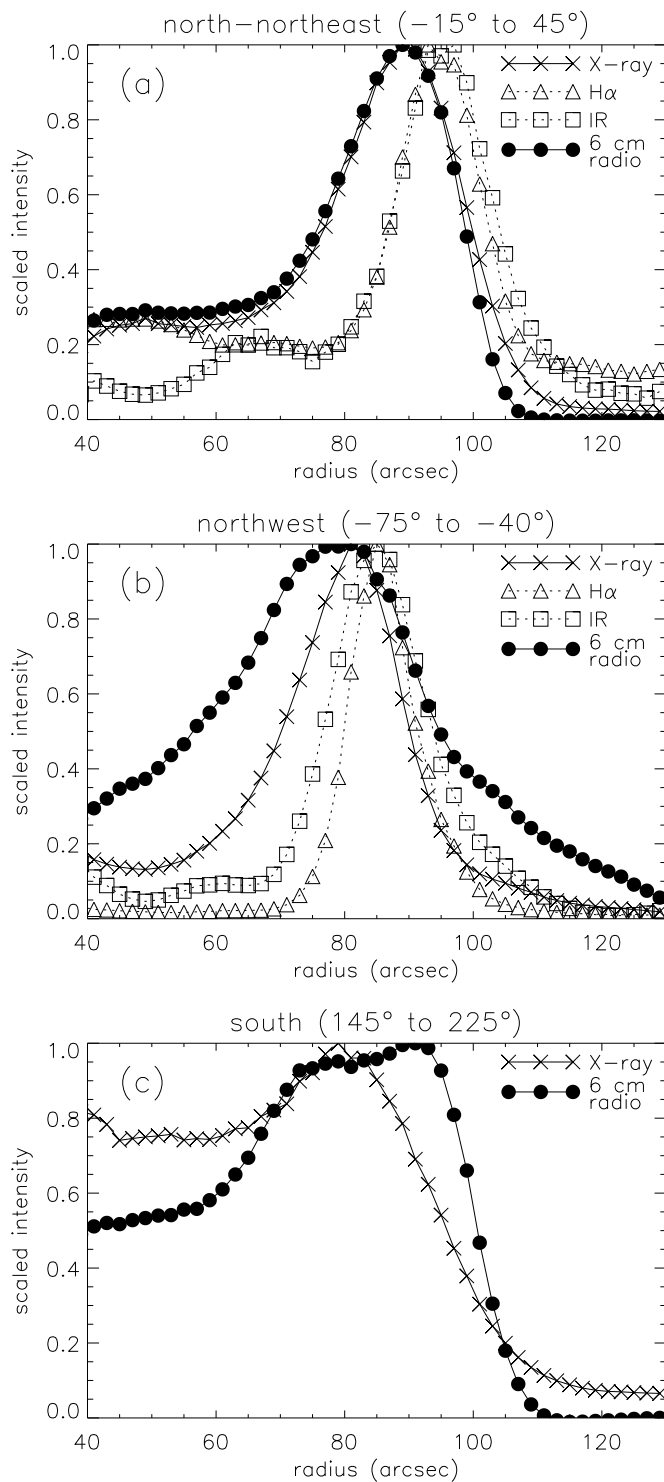


Fig. 15.— Angle averaged radial profiles at all wavebands for (a) the north to northeast (-15° to 45°), (b) the northwest (-75° to -40°), and (c) the southern (145° to 225°) regions. The center used for the azimuthal averaging is $\alpha_{2000} = 17^{\text{h}}30^{\text{m}}41^{\text{s}}.25$ and $\delta_{2000} = -21^\circ29'29''.7$.

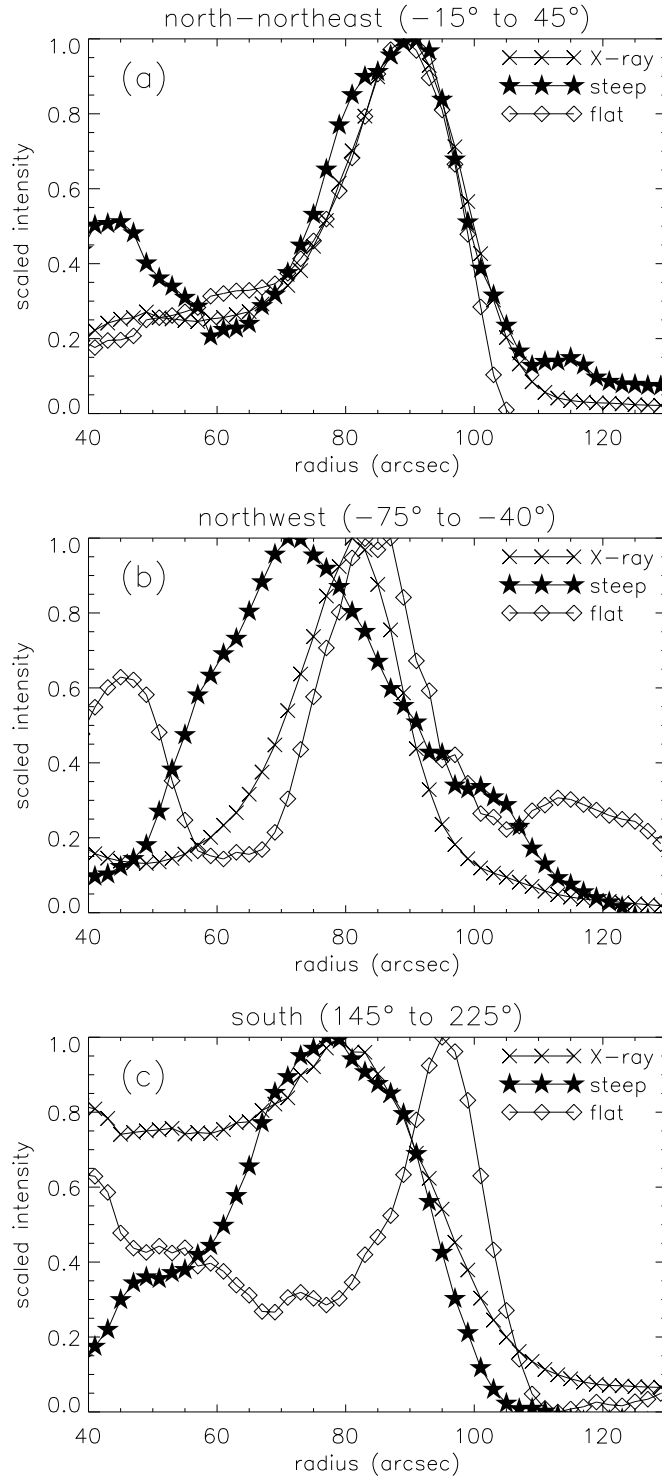


Fig. 16.— The same as Figure 15 for X-rays, flat-spectrum radio, and steep-spectrum radio.

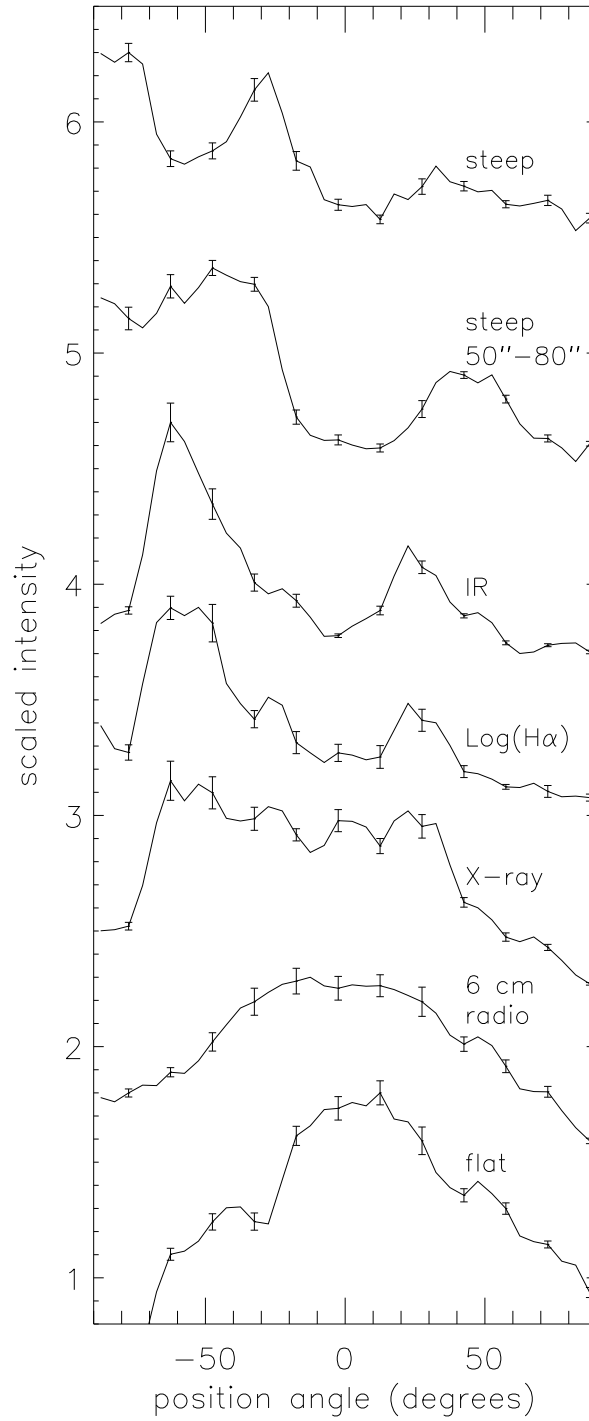


Fig. 17.— Intensity averaged every 5° in position angle for an annulus $70'' - 100''$ in radius around the northern ring. Note that the steep-spectrum radio emission has also been averaged in an annulus from $50'' - 80''$. The rms of the mean intensity is shown for every third independent azimuth bin. The center used for this plot is the same as that in Figure 15.